FACULTY OF SCIENCES

MODELLING THE EFFECT OF THE ROER VALLEY GRABEN BORDER FAULTS ON GROUNDWATER FLOW

THE CASE OF THE GROTE BROGEL FAULT

Albert Fernández Lagunas
Student number: 01811474

Promotor: Prof. dr. Thomas Hermans
Copromotor: Dr. Koen Van Noten, Royal Observatory of Belgium

Jury: Prof. dr. Kristine Walraevens, Jef Deckers

Master's dissertation submitted in partial fulfilment of the requirements for the degree of master in geology

Academic year: 2020-2021

GHENT UNIVERSITY

KU LEUVEN

“You miss 100% of the shots you don’t take”

- Michael Scott

Acknowledgements

What a journey it has been this dissertation. Sometimes a nightmare, sometimes a sparkling light. I guess every cloud has a silver lining and I have finally made it to the end. There is a popular expression in Spanish that says it is of good education to be grateful and, of course, there is a lot of people who I would like to thank for their support.

I would like to start by thanking both of my promotors, Prof. Hermans and Koen, who have guided me throughout the whole process, for their dedication, their advice, their support and their comprehension and patience. It could have not been possible to finish this piece of work without them. Even with the distance and a (too long) break for my part, we managed to work it out. Also, their feedback during the online meetings (from our home studios) was really helpful to make all the pieces come together.

My friends are definitely worth mentioning as well. Even though we have been separated by more than 1000 km for a while now, we have stayed in contact in a way or another, especially online (top trending in 2020). The different Geologica online events on the Discord server or on Zoom were really entertaining and great disconnection moments. Hopefully we can reunite sooner than later in Ghent and spend more time together. What a wonderful two years they have been in this beautiful city with all my friends, geologists and not geologists, Belgian, Spanish and International. I will surely remember all the good moments for years to come.

Although I have not been able to see them all as much as I would have liked, my friends in Barcelona have also been supportive and we have spent good moments together when the sanitary restrictions let us.

Last, but not least, to my parents for their unconditional support in everything. I do not know what it would be of me without them.

This study has been possible thanks to the academic license of the GMS (Groundwater Modeling System) software from Aquaveo™ and the Royal Observatory of Belgium for the provided monitoring data.

Table of content

The Story of my Research

Since high school I have always been interested in environmental sciences and studying the Bachelor in Geology at the University brought me even closer to this branch of the science. Taking part in an actual research program during my Bachelor Thesis, which was focused on nitrate contamination, was very interesting and I learnt a lot about it. However, for my Master Dissertation I have taken a different path. When this topic was proposed, I had just taken the course on Groundwater modelling in which I had put a lot effort. I found that the course had a useful application to real problems, so I decided to do my research using groundwater modelling tools to learn more about it and expand my knowledge on hydrogeology as well.

The best part of the research in this study is gaining knowledge on how faults and the hydrogeology are related by means of a 3D model. Such models allow to predict the responses of the aquifer to stress periods, which could be for example pumping due to a groundwater extraction. This allows to manage better our water resources and extract them in a more responsible way without damaging the aquifer system. Moreover, as transport of solute particles in groundwater can be also modelled, pollution problems could also be investigated.

However, building a groundwater 3D model can be quite challenging as there are a lot of sources from which errors can arise. Starting from the conceptual model to the numerical model, the grid definition and parametrization, everything is correlated. Once the parameters are calibrated with the field data, the model is able to produce similar responses to those observed and it could be used for prediction, for assessment or for testing. This broad range of applications makes groundwater modelling a really useful tool both for the professional world and research. For these reasons, I hope that this study will help in understanding better how to approach groundwater models as well as understanding the role of faults on groundwater. Because, who knows if I will have to deal with similar type of settings or use groundwater modelling in my future career as professional or as researcher.

a) Regional Flow

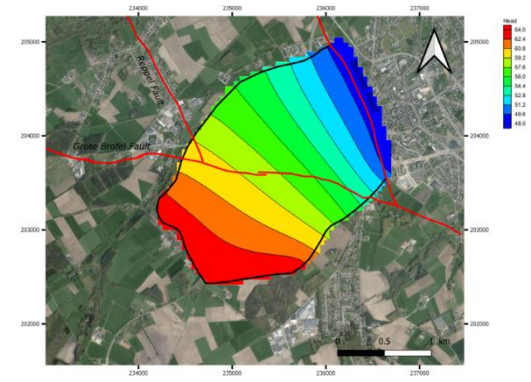

b) Regional Flow with the GBF

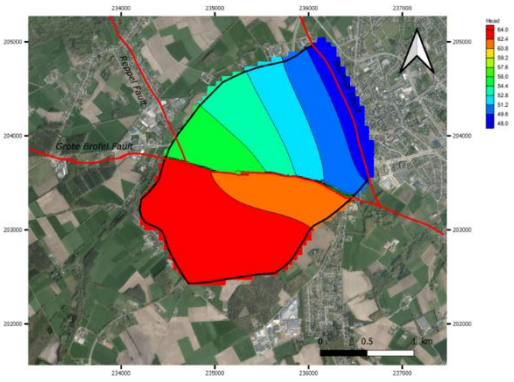

Abstract

The border faults of the Roer Valley Graben (RVG) have been reported to act as barriers to groundwater flow and altering its regional behaviour. At the location of these faults, high hydraulic gradients have been observed due to the low permeability of the fault zone. This study focuses on the Grote Brogel Fault (GBF), which is a major WNW-ESE striking normal fault in Belgium that diverges from the main NW-SE striking border fault system of the RVG. Deckers et al. (2018) conducted a study at two sites along the GBF, Maarlo and Bree, in which these authors integrated Electrical Resistivity Tomography (ERT), Cone Penetration Test (CPT) and borehole data. Monitoring data of the groundwater levels, which showed a large hydraulic head difference of up to 13 m as a result of the GBF acting as a flow barrier, is available for both sites. In one of the sites (Bree) a local stepover in the shallow subsurface was observed, affecting the groundwater levels in the different fault blocks (Deckers et al., 2018).

The aim of the present study is to investigate the role of the GBF on the local hydrogeological conditions, considering local fault complexities observed along this border fault. To achieve the main objective, a couple numerical groundwater models were conducted. A preliminary sensitivity analysis was performed to determine the parameters controlling the fault zone hydrogeological behaviour. With the obtained knowledge, the monitoring data from Maarlo was used for calibration and further validation of the model. Finally, a model was set up for the Bree site to test different fault linking scenarios and observe their response to groundwater flow.

The results of the sensitivity analysis showed that the thickness of the fault zone is the most crucial parameter controlling its behaviour. The hydraulic conductivity (K) is also a determining parameter as the ratio of the thickness and the K of the fault define the resistance to groundwater flow. Moreover, the ratio between the formation K and the fault K controls the steepness of the hydraulic gradient across the fault. Once calibration was achieved, the model was able to simulate the trends of the hydraulic head in the footwall and the hangingwall. The calibrated parameters are coherent with those discussed by Lapperre et al. (2019) for already existing groundwater models in the RVG. For the Bree site, the defined scenarios for the stepover pointed out differences in groundwater flow, specially between the soft-link and the hard-link scenarios. These differences could be observed in the field by installing a monitoring network with several piezometers. Some guidelines will be given for the installation of a larger monitoring network.

1. Introduction

Different studies (e.g. Bense and Van Balen, 2003; Bense et al., 2003a; Lapperre et al., 2019) have shown that the faults from the Roer Valley Graben (RVG) act as barriers to groundwater flow. This behaviour prevents water to flow from the footwall to the hangingwall and creates large hydraulic head differences between both sides of the fault. Recently, Deckers et al. (2018) focused on the morphological expression of the Grote Brogel Fault (GBF) and its hydrogeological characteristics by performing borehole and geophysical measurements, and monitoring the hydraulic head variations in both footwall and hangingwall. However, the dynamics of groundwater across the GBF are still poorly understood. The main objective of this study is to investigate the role of the GBF at a local scale by means of groundwater modelling and understand the effect it may have at a larger scale.

1.1. Geologic and hydrogeologic context

The Roer Valley Rift System (RVRS, sometimes also referred to as the Lower Rhine Graben) developed during the late Oligocene as the north-western branch of the Rhine Graben system, which is part of the European Cenozoic Rift System extending from west of the Alps to the North Sea (Deckers et al., 2018; Vanneste et al., 2013). The RVRS is located in the border area between the Netherlands, Germany and Belgium, and consists of a series of grabens and horsts, separated by northwest-southeast trending normal faults, that extend over a distance of ~200 km (Vanneste et al., 2013). According to Geluk et al. (1994), based on the subsidence pattern during the Cenozoic, the north-western branch of the RVRS can be divided into different tectonic units (Fig. 1), which are, from east to west: the Krefeld Block; the Venlo, Peel and Köln Blocks; the Roer Valley Graben (RVG) and the Erft Block; the Eastern and Western Campine Blocks; and the Brabant Massif.

The RVG is the central graben of the RVRS, has an asymmetric structure with a northwest-southeast trend and is ~145 km long (Geluk et al., 1994; Deckers et al., 2018). At the north-eastern side, it is bordered by a discrete fault zone, the Peel Boundary Fault, which presents total throws of up to 1000 m (Geluk et al., 1994). At the south-western margin, the RVG is bordered by a broad fault bundle, the Feldbiss Fault Zone (FFZ), which consists of a series of faults with a left-stepping pattern, and with total throws in the order of 100-400 m (Geluk et al., 1994; Deckers et al., 2018). In the Belgian sector of the RVG, in the vicinity of the town of Bree, the FFZ splits into three NNW-SSE trending faults. These faults are the NW-SE oriented Bocholt and Reppel Faults, and the WNW-ESE oriented Grote Brogel Fault (GBF). The total displacement is more or less equally divided between the three fault branches (Vanneste et al., 2001; Deckers et al., 2018).

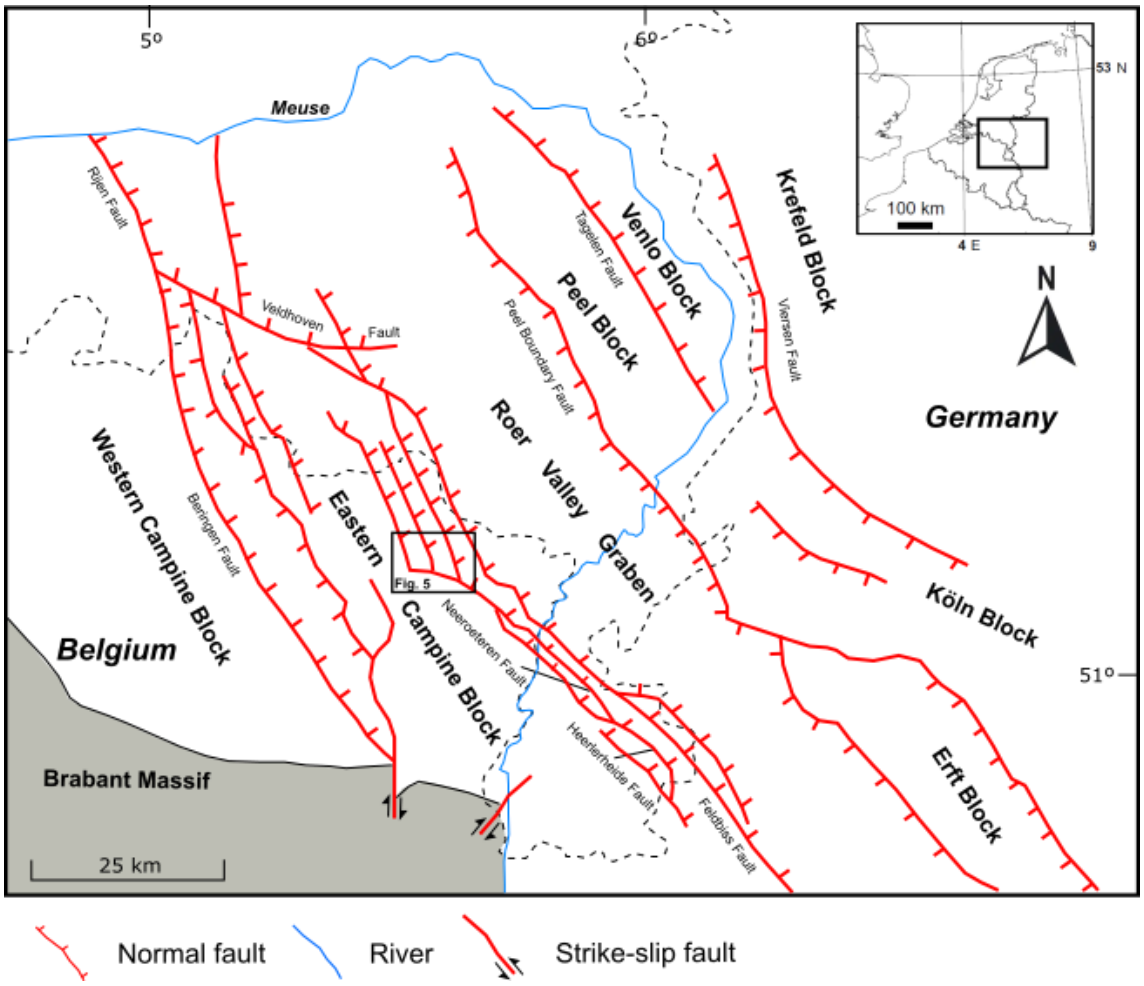

Figure 1. Structural framework of the Roer Valley Graben with the main blocks and faults displayed (after Geluk et al., 1994).

Quaternary to recent seismotectonic activity has been recognized in the RVRS area along the large border faults (e.g. Paulissen, 1997; Camelbeeck and Meghraoui, 1998). As a result of this activity, these faults have promoted the formation of geomorphological features at the surface, which generate a topographic relief in the form of a scarp (Camelbeeck and Meghraoui, 1998). The topographic relief generated by the fault's activity promotes groundwater flow from the footwall to the hangingwall (Deckers et al., 2018). Since the faults emplaced in the unconsolidated sediments in the RVRS represent a barrier to horizontal groundwater flow (Bense et al., 2003a). The hydrogeological behaviour of the faults in the RVRS causes the groundwater table in the footwall to be rather shallow. However, in the hangingwall causes a deeper groundwater table, which induces a large hydraulic head difference and a high hydraulic gradient over the fault line as it can be observed in Figure 2 (Bense et al., 2003a; Deckers et al., 2018; Lapperre et al., 2019).

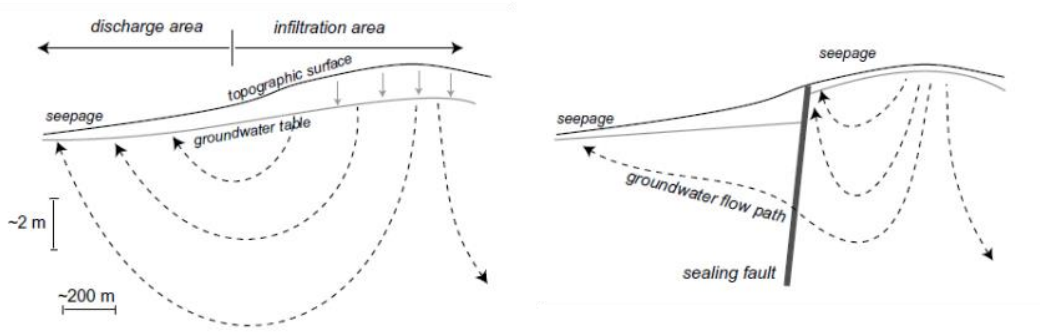

Figure 2. Conceptual graph showing difference in groundwater flow paths and groundwater table due to the presence of a fault acting as a flow barrier in a shallow aquifer (Bense et al., 2003a).

1.2. Fault zone characterization

From a hydrogeological point of view, faults and shear zones constitute very important types of discontinuities in rocks as they may affect hydraulic properties and therefore also the groundwater regime (Singhal and Gupta, 2010). Faults can act either as barriers, as conduits or as a combination of both that may enhance or impede fluid flow (Caine et al., 1996; Bense and Person, 2006). According to Bense et al. (2003b), the impact a fault has on fluid flow can be regarded as the sum of two different effects: the geometry of the different units (aquifers and aquitards which are juxtaposed at the fault) and the deformation processes in the fault zone, which may induce a change in the hydraulic properties of the material. The changes of properties may occur in and around a fault zone via deformation mechanisms along the fault (Bense et al., 2003b).

As faults play a major role in the groundwater regime in the RVG area, it is important to characterize them as accurately as possible. For this reason, knowledge over the existing fault zone models, deformation mechanisms and their effect on hydraulic properties is important and they will be shortly reviewed in the following sections.

1.2.1. Deformation mechanisms

Massive crystalline rocks have generally a very low porosity and permeability. Nevertheless, the presence of fractures and discontinuities in this type of rocks, may enhance the occurrence and movement of groundwater through them (Singhal and Gupta, 2010). These fractures, when open, form passages for groundwater. However, if they are filled with weathered or broken rock material and clays, their permeability is reduced (Singhal and Gupta, 2010). Crystalline rocks are not part of the studied aquifer systems in the RVG, which are composed mainly of unconsolidated sediments (Bense et al., 2003b). Therefore, deformation mechanisms in crystalline rocks will not be reviewed in this study.

In clean sands, three different brittle deformation mechanisms can occur in function of the burial depth and the matrix porosity (Fig. 3a; Fulljames et al., 1997). These mechanisms are named cataclasis, particulate flow and clastic flow (Bense et al., 2003b). As clastic flow only occurs at larger depths (Bense et al., 2003b), it will not be discussed in this section as only the first two mechanisms are relevant for this study, which focuses on the shallow part of the faults. At shallow

depths (less than 1 km) particulate flow will be the dominant deformation mechanism (Fig. 3a). During particulate flow, the grains roll past each another without crushing, while the pores within the fault zone tend to dilate, disaggregating the grain fabric (Fig. 3b; Fulljames et al., 1997; Bense et al., 2003b). These loose particles generated by friction due to abrasive wear in the fault plain are known in literature as gouge (Scholz, 2002). According to Fulljames et al. (1997), if no significant diagenetic processes take place, the resulting fault gouge properties do not differ significantly from the surrounding matrix (Fig. 3b). At depths greater than ~1 km, cataclasis is the dominant mechanism and it consists on the crushing of sand grains, which leads to a significant grain size reduction within the fault zone (Fulljames et al., 1997; Bense et al., 2003b). Contrary to the particulate flow, the hydraulic conductivity from the resulting fault gouge is largely reduced. The reduction is larger perpendicular to the deformation band than along the strike (Bense et al., 2003b; and references therein).

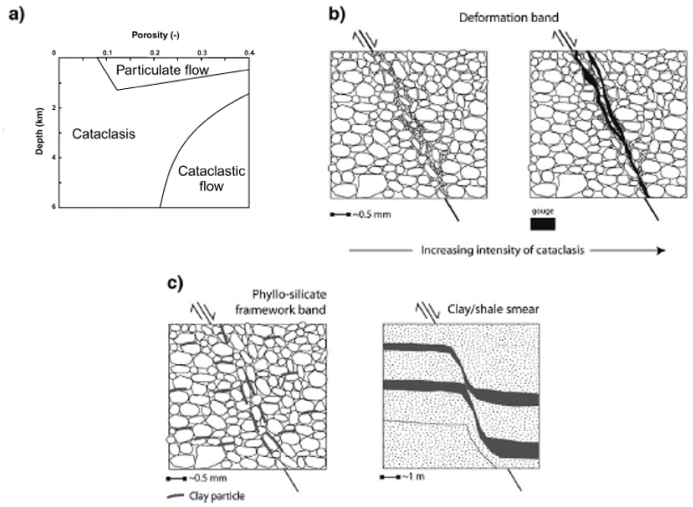

Figure 3. a) Dominant deformation process according to depth and mean poroity (Bense et al., 2003b; after Fulljames et al. 1997). b) Deformation bands created as a result of particulate flow due to cataclasis. c) Clay beds fold along the fault giving place to clay smear (Bense et al., 2013).

In sedimentary successions where clay layers are present, the introduction of clay into the fault is one way of strongly reducing the effective hydraulic conductivity of the fault zone. Dragging or ductile flow of the clay layers along the fault plane between the up- and down-thrown source beds can result in a clay smear along the fault plane (Fulljames et al., 1997; Bense et al., 2003b). The smear forms a layered gouge containing clay from each source bed (Fig. 3c). According to Fulljames et al. (1997), the thicker the source beds are, within the throw window, the greater the thickness of the smear is. Therefore, a thicker smear is more likely to be continuous across the fault zone, while a thinner smear is more likely to be discontinuous.

Diagenetic processes such as the precipitation of minerals composed of, for example, iron (Fe) and manganese (Mn) oxides or calcite ($CaCO_3$), can cement and, thus, seal a permeable fault plane by partially or completely reducing its porosity (Knipe, 1993; Bense et al., 2003b). Although many seals involve a combination of diagenetic processes, it is often possible to identify one that dominates. These processes of porosity reduction can occur at different rates, allowing the high

permeability window associated with faulting to remain open for different stages of evolution (Knipe, 1993).

1.2.2. Fault zone architecture

According to the fault zone architecture model proposed by Caine et al. (1996), the primary components of which a fault is build up are the fault core, the damage zone and the protolith or undeformed part of the host rock (Fig. 4). These components may not always be present, and in addition, depending on the stage of the fault evolution, their fluid flow properties may change (Caine et al., 1996).

The fault core is defined as the structural, lithologic and morphologic part of a fault zone where most of the displacement is accommodated, and which presents the most shear deformation (Caine et al., 1996; Bense et al., 2003b). Fault cores may include slip surfaces, unconsolidated clay-rich gouge zones, brecciated and geochemically altered zones or cataclastic zones (Caine et al., 1996; and references therein). Thickness variations down dip and along the strike, combined with its internal structure, may play an important role in controlling the fluid flow properties of fault cores. Moreover, grain-size reduction and/or precipitation of minerals due to deformation mechanisms, could lower its porosity and permeability compared with the protolith leading to fault cores acting as barriers to fluid flow (Caine et al. 1996, see section 1.2.1).

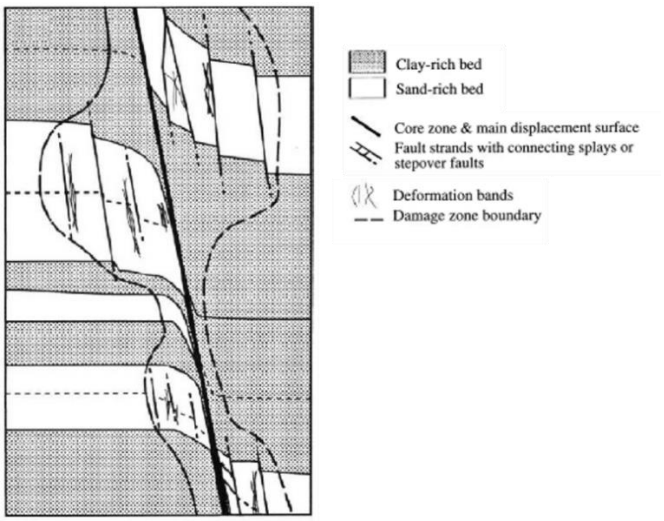

Figure 4. Fault zone architecture model proposed by Caine et al. (1996), where the different elements forming the damage zone can be observed.

The damage zone forms the intermediate region between the fault core and the undisturbed protolith (Bense and Person, 2006). In damage zones, fault-related structures such as small faults, veins, fractures, cleavage and folds can be found. These structures accommodate most of the deformation in the damage zone (Bense et al., 2003b) and cause heterogeneity and anisotropy in the permeability structure and elastic properties of the fault zone (Caine et al., 1996). In addition, a mixing zone between the damage zone and the fault core could develop due to mixing and rotation of sandy and clayey material at the grain scale (Heynekamp et al., 1999;

Rawling et al., 2001). These processes result in a porosity reduction of the grain fabric (Heynekamp et al., 1999; Bense et al., 2003b). Damage zones along faults in unconsolidated sediments do not contain open-fracture networks and therefore, they have little potential as vertical-flow conduits. They have a stronger effect on horizontal flow than faults containing open fractures instead (Rawling et al., 2001; Bense et al., 2003b). Furthermore, different studies have confirmed that its thickness may depend on the type of protolith where the fault is emplaced. While Bense et al. (2003b) studied the deformation mechanisms in unconsolidated sediments in the RVG and reported a rather small damage zone of up to 4 m thick, Micarelli et al. (2006) studied the deformation mechanisms in a carbonate series, reporting a damage zone of up to 100 m thick.

1.2.3. Hydraulic characterization

The easiest way to quantify the hydraulic properties of a fault zone is to calculate its specific resistance (*c* [T]) to flow perpendicular to the fault zone. Bense et al. (2003a) describe it as the ratio of the fault zone width (*w* [L]) and the bulk hydraulic conductivity (*K* [LT^{-1}]) of the fault zone material:

$$c = \frac{w}{K} \text{ [T]} \qquad (1)$$

Darcy's Law is the expression of the rate of horizontal groundwater flow through an aquifer with a thickness *D* [L], length *L* [L], and hydraulic conductivity in the direction of flow *K* [LT^{-1}] (Bense et al., 2003a):

$$q = -KD\frac{\Delta h_L}{L} \text{ [L}^2\text{T]} \qquad (2)$$

Where Δh_L [L] is the head difference along the distance *L*. When *L* is equal to *w*, and there is continuity of flux across the fault, combining equation 1 with Darcy's Law (eq. 2), the resistance of a fault zone is obtained (Bense et al. 2003a; eq. 3):

$$c = D\left|\frac{\Delta h_{fault}}{q}\right| \text{ [T]} \qquad (3)$$

Where Δh_{fault} is the hydraulic head difference over the fault. The specific flow resistance to flow perpendicular to the fault zone is the most general form to characterize the hydraulic properties of a fault zone as they are gathered into a single parameter (Bense et al., 2003a).

1.2.4. Faults in groundwater modelling

Among the most common used finite-difference simulation programs, there are different numerical methods to implement a fault zone into hydrogeological models, resulting in a variety of solutions and ranges of results (Harte et al., 2006). The two primary methods are direct and indirect representations of the fault or barrier (Hornerberg et al., 2002; Harte et al., 2006). In the direct methods (e.g. discrete fracture network modelling and continuum approach), the hydraulic properties and physical dimensions of the fault zone are represented by the properties assigned to the grid cells that coincide with its location within the aquifer (Harte et al., 2006). In addition, the offset of hydro-stratigraphic units is generally implemented in conjunction with the fault zone to account to horizontal heterogeneity induced by the fault (e.g. Bense and Person, 2006). This

approach is often used for fluid flow models along fault zones in sedimentary basins considering regional scale (~10-100 km) and more local (~1-5 km) groundwater flow systems (Bense et al., 2013; and references therein). Due to the fact that fault zones are usually narrow compared to the scale of the groundwater-flow system, this approach may require a very fine grid and thus, become computationally expensive (Hornerberg et al., 2002; Harte et al., 2006). In the indirect method, the intercell hydraulic conductance is adjusted for cell faces coinciding with the barrier location to represent the hydraulic properties of the barrier (Harte et al., 2006). The objective of this approach is to represent primarily the properties of the barrier rather than the properties of the adjacent cells, in which the aquifer properties are assigned (Harte et al., 2006). Different studies have taken this approach described by Hsieh and Freckleton (1993) using the Horizontal Flow Barrier (HBF) package to model solute transport across a flow barrier (e.g. Hornerberg et al., 2002; Harte et al., 2006).

Turnadge et al. (2018) reviewed the methodologies for fault implementation in groundwater flow models for coal seam gas-related impact assessment in Australia. They identified that the representation of fault zones in models is still rare nowadays. Concerning the study area, Lapperre et al. (2019) discussed three different calibrated groundwater models of the RVG and how they implemented the faults. However, there are some models in the RVG which do not consider the implementation of faults. An example may be the study of VMM (2008) in the Maas area, for which a groundwater model was built without representing the RVG border faults present within the model. In addition, the effect of the geometry and property of faults at the local scale has rarely been studied using explicit groundwater models.

1.3. Groundwater modelling

A model can be defined as a simplified representation of a real system or process (Konikow and Bredehoeft, 1992; Loudyi, 2005). Two different kinds of models have been developed by researchers: physical and mathematical models. Mathematical models are based on the fact that the aquifer system and its behaviour can be represented by a set of mathematical expressions, such as partial differential equations, and can be classified as deterministic or stochastic (Loudyi, 2005). The stochastic approach is used, by assuming that the flow and transport parameters are random variables, to address uncertainty directly (Loudyi, 2005 and references therein). Quantitative descriptions of the considered variable field are generated and the results are given in the form of a probability density function (Loudyi, 2005).

Using a deterministic approach to the mathematical model, the governing equations can be solved analytically or numerically. Although exact solutions can often be obtained analytically, this requires that the parameters and boundaries are highly idealized. As deterministic groundwater models generally require the solution of partial differential equations and need discretization of space and time to account for varying property or stress factors (such as recharge or pumping rate), numerical models are seen as a more realistic and flexible approach than analytical solutions, even though they only provide approximate solutions (Konikow and Bredehoeft, 1992). Therefore, numerical models have become the most widely used approach, a trend accelerated

by the fast development and availability of high-performance computers (Loudyi, 2005). Due to this fact, the field of hydrogeology has turned toward numerical model simulations in order to help evaluating the groundwater resources (Gorelick, 1983).

Numerical models provide a framework for conceptualizing and evaluating aquifer systems. This has enabled to develop a better understanding of the functioning of regional aquifers and to test hypothesis regarding the behaviour of particular facets of groundwater systems in the field of hydrogeology (Gorelick, 1983). The modelling efforts can have, according to Loudyi (2005), three different objectives: (1) predicting the effect of certain actions given the field conditions, (2) interpreting system dynamics by gaining insight into controlling parameters, and (3) if data are insufficient, guiding data collection activities by means of generating geological conditions to analyse flow in hypothetical aquifer systems and, formulate guidelines for a specific region.

Because of the intrinsic complexity and heterogeneity of geological systems, most aquifers are complicated to describe accurately and therefore, the construction of a groundwater model is based on a set of assumptions, which simplify the real system (Loudyi, 2005; Bear and Cheng, 2010). The construction of a conceptual model, therefore, consists of identifying this set of assumptions describing the system composition, the relevant medium properties and the flow process mechanism. Extensive information on the natural system and collection of field data are essential to define more clearly the flow problem (Loudyi, 2005). These simplified versions must be satisfactory in view of the modelling objectives, the associated management problem and the available data (Bear and Cheng, 2010). Assumptions during the construction of a groundwater model are related to characteristics such as the hydrologic and stratigraphic domains including the definition of equivalent properties and the simplification of the heterogeneity, the dimensionality of the model (one, two or three dimensions), the geometry of the boundary in the domain of interest, the distribution of parameters, the behaviour of the system (steady-state or transient-state), the kind of soil or rock materials comprising the domain and the stresses (sources and sinks), among others (Loudyi, 2005; Bear and Cheng, 2010). Of course, these assumptions might generate discrepancies between observed and predicted responses of a system, which are the manifestation of errors in the mathematical model. Thus, when applying groundwater models to field problems, there can be three different sources of error. According to Konikow and Bredehoeft (1992) these error sources can come either from conceptual errors including all the categories described above, numerical errors arising from the equation solving algorithm or to uncertainties and inadequacies in the input data. Because of these difficulties, calibration and sensitivity analysis are brought as steps into the modelling process. Calibration is the process during which model parameters are updated to minimize the misfit between observed and calculated data. Sensitivity analysis aims at identifying the model parameters which have the larger influence on the data. These steps are tools which help to make sure that a model correctly describes all relevant processes to an acceptable degree of accuracy, and to evaluate the impact of uncertainty in the values of model coefficients (Bear and Cheng, 2010).

1.4. Problem definition

The presence of faults in hydrogeological systems can modify the groundwater flow regime as faults form discontinuities. As it has been shown in the previous sections, faults can act as barriers or conduits to water flow. Various studies have focused on the role of faults in the hydrogeological behaviour of the RVG (e.g. Bense et al., 2003a, b; Lapperre et al., 2019), showing that most of the faults in this area impede groundwater from flowing through them. This is indeed the case of the GBF, which is the object of study in this thesis. Deckers et al.(2018) showed that the water table was shallower in the footwall than in the hanging wall due to the presence of the GBF in the study area. In addition, Deckers et al. (2018) also suggested that the fluctuations of the water table in the foot wall are correlated with the precipitation events, while the changes in the hanging wall result from infiltration and water flowing through the fault from the foot wall.

1.5. Objectives

To date, the dynamics of groundwater flow across the GBF is still poorly understood. Therefore, the general aim of the present study is to investigate the role of the GBF on the local hydrogeological conditions, considering local fault complexities observed along this border fault. More generally, comprehensive studies of the effect of faults, including their shallow geometry, on local flow systems are lacking in the literature. We propose a sensitivity analysis of such a fault system using a synthetic benchmark followed by a field application on the GBF. The results of this investigation will be then extrapolated to a larger scale in order to understand better the hydrogeological dynamics not only of the GBF, but also of the neighbouring graben faults. To reach the main goal of this study, various sub-topics are considered, from which the following specific research questions are addressed:

1. Which are the parameters that control the hydrogeological dynamics in aquifers affected by fault systems?
2. Can the hydrogeological parameters of the GBF be derived from the available information?
3. Is it possible to predict accurately the hydrogeological dynamics through a determined time span in this type of geological setting?
4. Can local structural complexities be solved by means of groundwater modelling?
5. How can field data be gathered in this type of setting to characterize better the impact of flow-barrier faults on groundwater flow?
6. Should faults be explicitly included in large scale groundwater models?

2. Site description

2.1. Geomorphologic setting

This study focuses on two different sites (Maarlo and Bree; Fig. 5), both situated in the province of Limburg in Belgium, close to the border with The Netherlands. These sites are located along

the GBF, a little westward from where the FFZ splits into three different segments. The presence of these faults generates a topographic relief composed geomorphologically of plains and plateaus, which are separated by important slopes (Beerten et al., 2005). South of Bree, the Campine Plateau rises above the surroundings up to an elevation of 70-75 m above sea level[1]. The Campine Plateau is cut by several valleys with a southwest-northeast direction (Fig. 5). In the northern direction, the relief lowers in steps due to the presence of the Grote Brogel, the Reppel and the Bocholt faults. These steps generate, from west to east, the Kaulille Plain with a mean altitude of 50 m, the Reppel Plain at 45 m altitude, and the Bocholt Plain at 35-40 m altitude (Fig. 5; Beerten et al., 2005). The NW-SE border of the Campine Plateau is the most prominent feature and has been recognized as an active tectonic fault scarp with a denivelation of 20 to 25 m (Paulissen, 1997; Camelbeeck and Meghraoui, 1998). The Bree scarp (as it is named) coincides at the surface, on different sections, with the prolongation of the FFZ and it must be considered as the morphological expression of the fault's recent tectonic activity (Camelbeeck and Meghraoui, 1998).

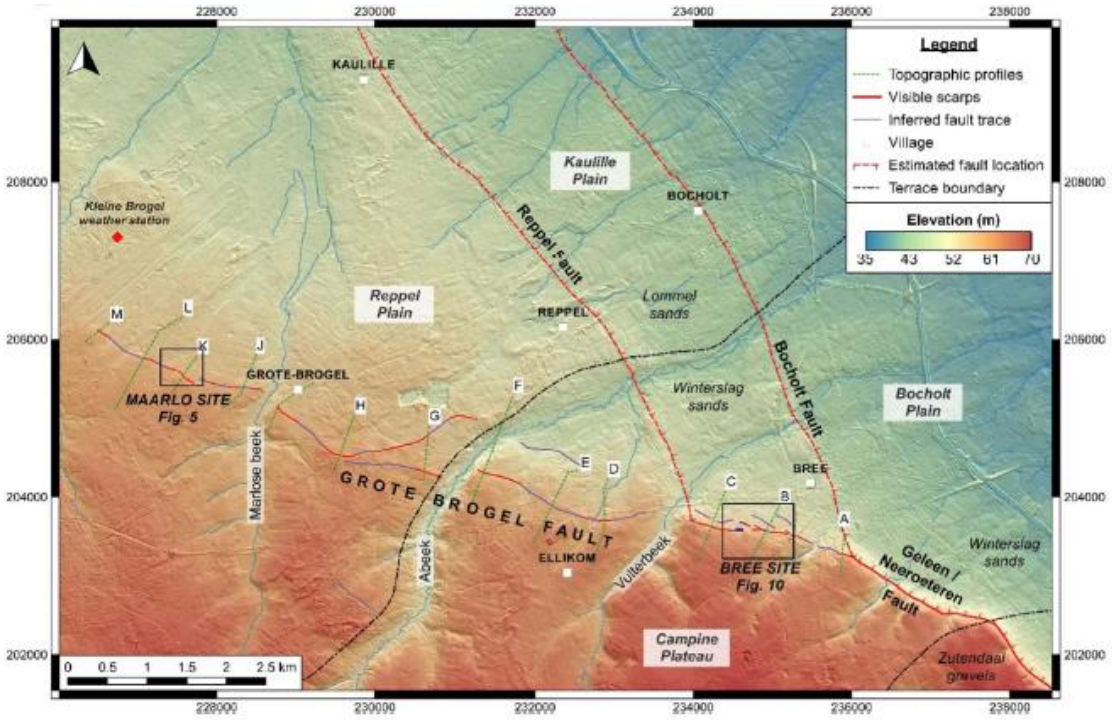

Figure 5. Morphotectonic map of the RVG border faults with the indication of Maarlo and Bree sites. Labels A to M correspond to topographic profiles (Deckers et al., 2018). Coordinates in Belgian Lambert 1972.

The GBF is best expressed in the easternmost section between the bifurcation with the FFZ and Bocholt fault near Bree and the Vulterbeek, where a prominent scarp is present (Fig. 5). According to Deckers et al. (2018), this scarp appears to be contiguous with the Bree scarp as there is no geomorphic breaks between both scarps. This scarp is rather steep in the extreme east but rapidly broadens towards the west, as its height is reduced. In the section between the Vulterbeek and

[1] m above sea level (m.a.s.l.) will be used for topography and water levels in this report.

Abeek, the fault trace blurs, and no clear scarps can be identified. However, an important complexity in the surface trace of the GBF is observed in the section between the Abeek and the Maarlose beek, where two scarps with a different strike can be seen (Deckers et al., 2018). In this case, the total topographic offset should be divided between both segments. Two sites along the GBF have been selected for this study, the Maarlo and Bree Sites (Fig. 5), which were previously studied by Deckers et al. (2018) and will be described further in this section.

2.2. Stratigraphy

During the Mesozoic and Cenozoic, the RVG was characterized by several episodes of subsidence (rifting) and inversion (Geluk et al., 1994; Deckers et al., 2018). The latest episode of rifting initiated in the RVG in the late Oligocene and was characterized by dense small-displacement faulting in the graben, but faults rapidly grew into long systems (Deckers, 2016). A thick succession of unconsolidated sediments accumulated from the start of the late Oligocene rifting onwards. Fine-to-medium grained marine deposits from the Late Oligocene to the latest Miocene are overlain by Plio- and Pleistocene medium-to-coarse grained estuarine-fluvial-deltaic deposits, reaching a maximum thickness of up to 1200 m in the northern part of the graben (Michon and Van Balen, 2005; Deckers et al., 2018).

During the Miocene, a large delta system prograded in the RVG during which the Breda Formation (hereafter the abbreviation Fm will be used) was deposited in the study area (Vandenberghe et al., 2014). This formation is the Dutch equivalent for the Kasterlee Fm and consist of slightly glauconitic, medium grained marine sands (Dusar et al., 2001). The delta growth in the primeval rivers Rhine and Meuse continued during the Pliocene and early Pleistocene, when the deposition of the estuarine to fluvial Mol Fm occurred (Fig. 6). This formation is divided in two halves, a lower and an upper half. The lower half consists of coarse-grained white quartz-rich sands, while the upper half consists of lignite-clay and sand (Dusar et al., 2001; Deckers et al., 2018). During the late Pleistocene, the Mol Fm was covered by the deposition of coarser fluvial deposits (coarse sands with gravels) of the Meuse Group by the action of the Rhine and Meuse Rivers (Deckers et al., 2018). In the downthrown block, these coarse sands were eroded by the Rhine, which afterwards deposited the Bocholt and Lommel sands (Fig. 6; Camelbeeck and Meghraoui, 1998). The Winterslag sands in contrast, show an origin affinity towards the Meuse river (Deckers et al., 2018 and references therein). Middle Pleistocene tectonic activity forced the Rhine-Meuse river system to leave the RVG, causing a shift in the sediment sequences from a dominance of fluvial processes to predominantly aeolian (Schokker and Koster, 2004). These deposits are gathered in the Gent Formation (Fig. 6; Deckers et al., 2018).

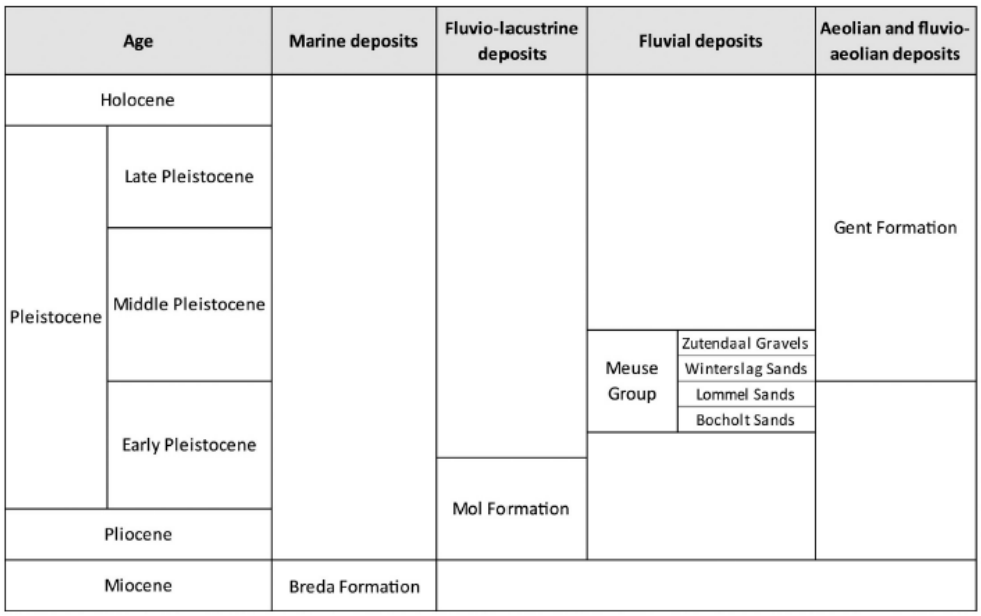

Figure 6. Summary of the lithostratigraphic units in the study area with its age and the depositional environment (after Deckers et al., 2018). Only the quaternary units (Gent Fm, Meuse Gr and Mol Fm) will be considered in this study for modelling purposes.

2.3. Maarlo site

At this site (Fig. 7a), the fault scarp presents a maximum height of 5.4 m, is very broad without a clear break (Fig. 7b), decreasing progressively between 2 and 7 km. Due to these characteristics, the precise position of the GBF at the surface in this site is not obvious from the morphology (Deckers et al., 2018). Although no trenches have been digged at Maarlo, Deckers et al. (2018) conducted a study at this site which included the recording of two collinear Electrical Resistivity Tomography (ERT) profiles. Along one of the ERT profiles, seven Cone Penetration Tests (CPT) were conducted. In addition, two boreholes were drilled at the same location as two of the CPTs, one on each side of the fault. The location of the ERT profiles, the CPTs and the boreholes is displayed in Figure 7a.

ERT, CPT and borehole data from Deckers et al. (2018), show that two main units are present in the Maarlo site (Fig. 8). A first unit which presents a high electrical resistivity and is sub-horizontal, and a second one which presents a low-to-medium resistivity. Both units are brought in contact by the presence of a single normal fault throwing to the NNE, which is outlined by a strong lateral contrast in electrical resistivity (Fig. 8a). The high resistivity layer is thicker in the hanging wall of the fault than in the footwall. In the hanging wall, is thickness varies between 10 and 12 m, while in the footwall varies from less than 1 m to 3-4 m (Deckers et al., 2018). The correlation between ERT (gathered in autumn 2015) and CPT profiles shows that the high resistivity layer is a coarse-grained lithology, while the low-to-medium resistivity layer would be composed of a finer-grained lithology (Fig. 8b). These two units, according to Deckers et al. (2018), correspond to the Meuse Group (coarse-grained and high electrical resistivity) and the Mol Formation (finer-grained and low-to-medium electrical resistivity).

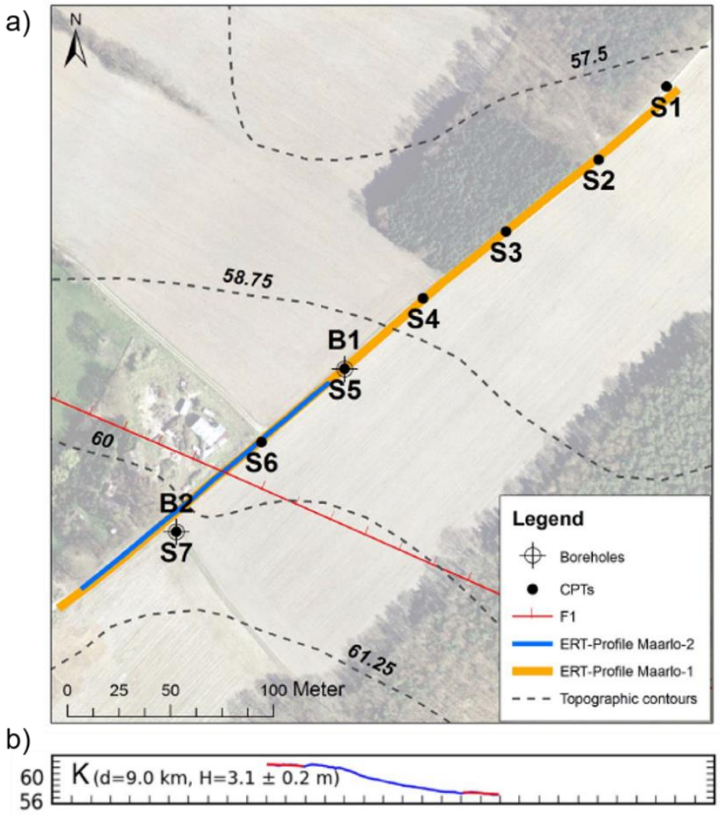

Figure 7. a) Maarlo site, with the location of the fault, the boreholes, the CPTs and ERT-profiles displayed. b) Topographic profile K of the Maarlo site (for location see Fig. 5). After Deckers et al. (2018).

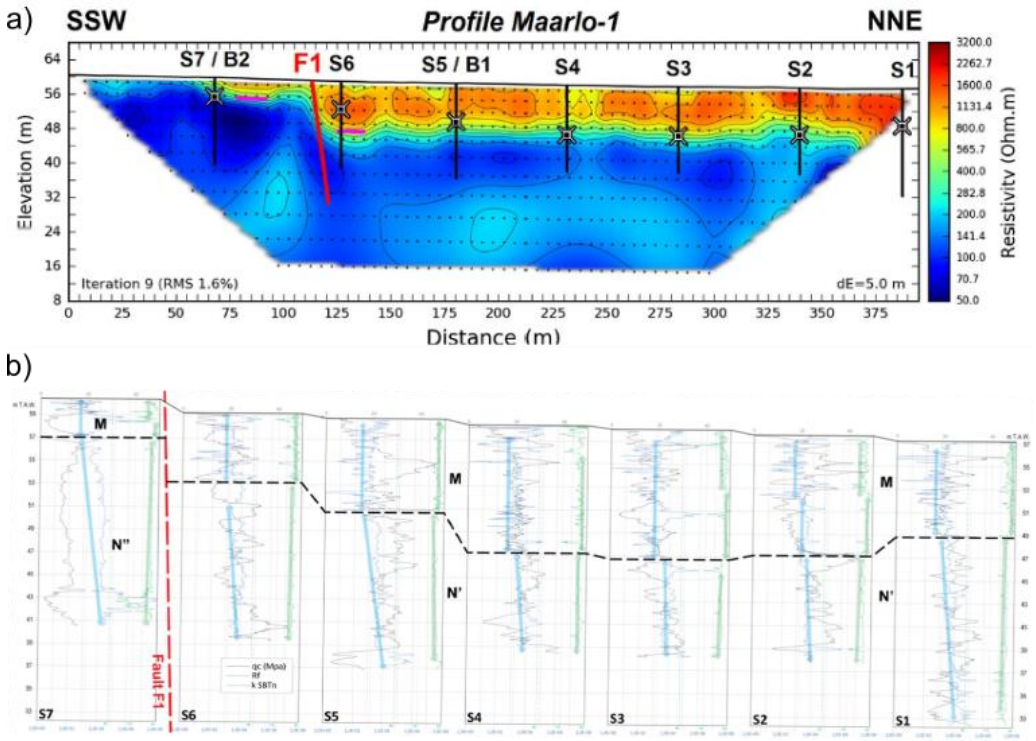

Figure 8. a) ERT-profile Maarlo-1 showing the resistivity of the different geological units and the contrast created by the fault (F1). b) Correlation between the different CPTs by Deckers et al. (2018).

Groundwater levels were also monitored by Deckers et al. (2018) during a period of 10 months (November 2015 to September 2016). The average groundwater level through this period in the footwall was 59.3 m while in the hangingwall was 53.5 m. Monitoring showed that the water table was shallower in the footwall than in the hanging wall, and that the average groundwater level was 6 m higher in the foot wall due to the presence of the fault. In addition, Deckers et al. (2018) compared the fluctuation of the groundwater level with precipitation data from the zone gathered at the Kleine Brogel Station (Fig. 9). According to these authors, the water table changes in the foot wall are correlated with the rainwater supply, aligning and correlating with the rainfall peaks, while in the hanging wall these changes are smoother. Deckers et al. (2018) also suggest that the changes in the hangingwall result from infiltration from the surface and water flowing through the fault, which originated in the foot wall.

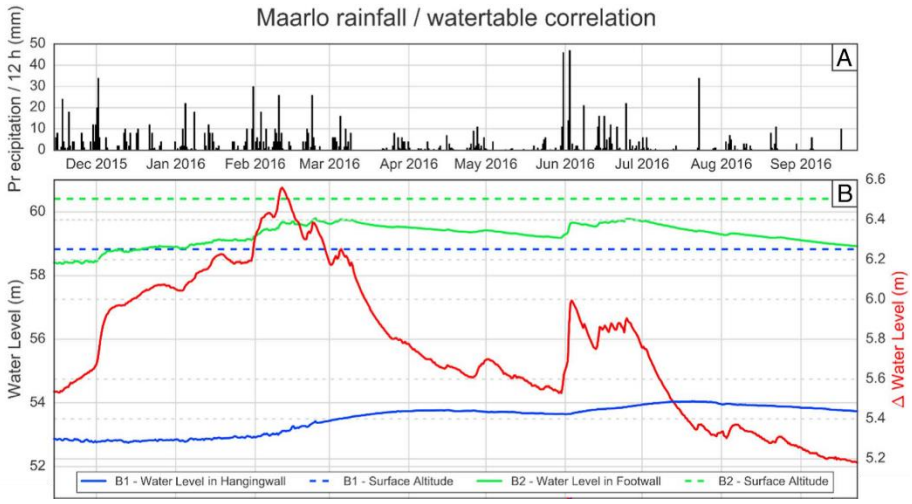

Figure 9. a) Precipitation measured at the Kleine Brogel Station and averaged every 12 h. b) Groundwater table results of the monitoring in the footwall (green line) and the hangingwall (blue line). The red line represents the head difference between the two walls of the fault (Deckers et al., 2018).

2.4. Bree Site

Deckers et al. (2018) defined two subsites at Bree. For this study, the focus will be set on the western subsite, where two fault splays (F2 and F3) were observed (Fig. 10). At this subsite, Deckers et al. (2018) performed multiple ERT profiles and CPTs, and two boreholes, whose locations are displayed in Figure 10. The fault scarp in this subsite is relatively broad without steep gradients, while to the east it becomes very pronounced (Deckers et al., 2018). The groundwater level was also monitored from February 2016 to March 2016 at the two boreholes (B3 and B4). Additionally, six hand auger (HA) borings were drilled by Deckers et al. (2018) along an ERT profile to investigate the influence of the fault splays on groundwater.

Figure 10. Aerial photograph of the Bree Site with the location of the ERT-profiles, the CPTs, the boreholes and the hand auger borings displayed, as well as both fault splays (Deckers et al., 2018).

Deckers et al. (2018) defined five distinct units in the CPTs (Fig. 11a), corresponding to the sedimentary succession of the Gent Fm, Meuse Gr and the Mol Fm. This sedimentary succession can be found in both the footwall and the hanging wall. However, in the hanging wall (borehole B3) of both fault splays (F2 and F3), the Gent Fm and Meuse Gr are much thicker and the facies of the Mol Fm is different from the footwall (borehole B4). In the footwall, the aelonian sands of the Gent Fm are on top of the coarse gravel-bearing sands of the Meuse Gr, and both correspond to high resistivity unit (Fig. 11b; Deckers et al., 2018). Deckers et al. (2018) identified the fine silty-sandy facies of the basal part of the Mol Fm as the medium-to-low resistivity unit. At the top of the hanging wall, the medium to high resistivity values correspond to the lower part of the Gent Fm (Fig. 11b). Deckers et al. (2018) attribute this heterogeneity to the fine-grained nature (fine loamy sands) of the geological formation. Below the Gent Fm, high to very high resistivity values arise due to the presence of the coarse sands from the Meuse Gr. The last unit according to Deckers et al. (2018) corresponds to the lignite-bearing silty medium sands of the upper part of the Mol Fm, and presents medium resistivity values. These correlations by Deckers et al. (2018) showed that the thickness of the Gent Fm and the Meuse Gr increase from the footwall to the hanging wall of F3: from ~0.5 to ~3 m for the Gent Formation, and from ~5 to ~13 m for the Meuse Group.

These layers are offset by two fault splays, a norther one (F3), which accommodates most of the offset, and a southern one (F2) with a minor offset (Deckers et al., 2018). Deckers et al. (2018) recognized in the ERT profiles (Fig. 12) that the two fault splays form an overlapping system with compensating offset. F3 is the main splay and it is likely to connect eastward with the single splay that Deckers et al. (2018) observed in the eastern subsite. Nevertheless, the offset of F3

decreases abruptly to the west of Bree-6, where F2 becomes the main splay and connects with the fault observed in Bree-1 (Fig. 12). Therefore, the main slip transfer occurs between profiles Bree-2 and Bree-7, in a 25-30 m wide zone (Deckers et al., 2018).

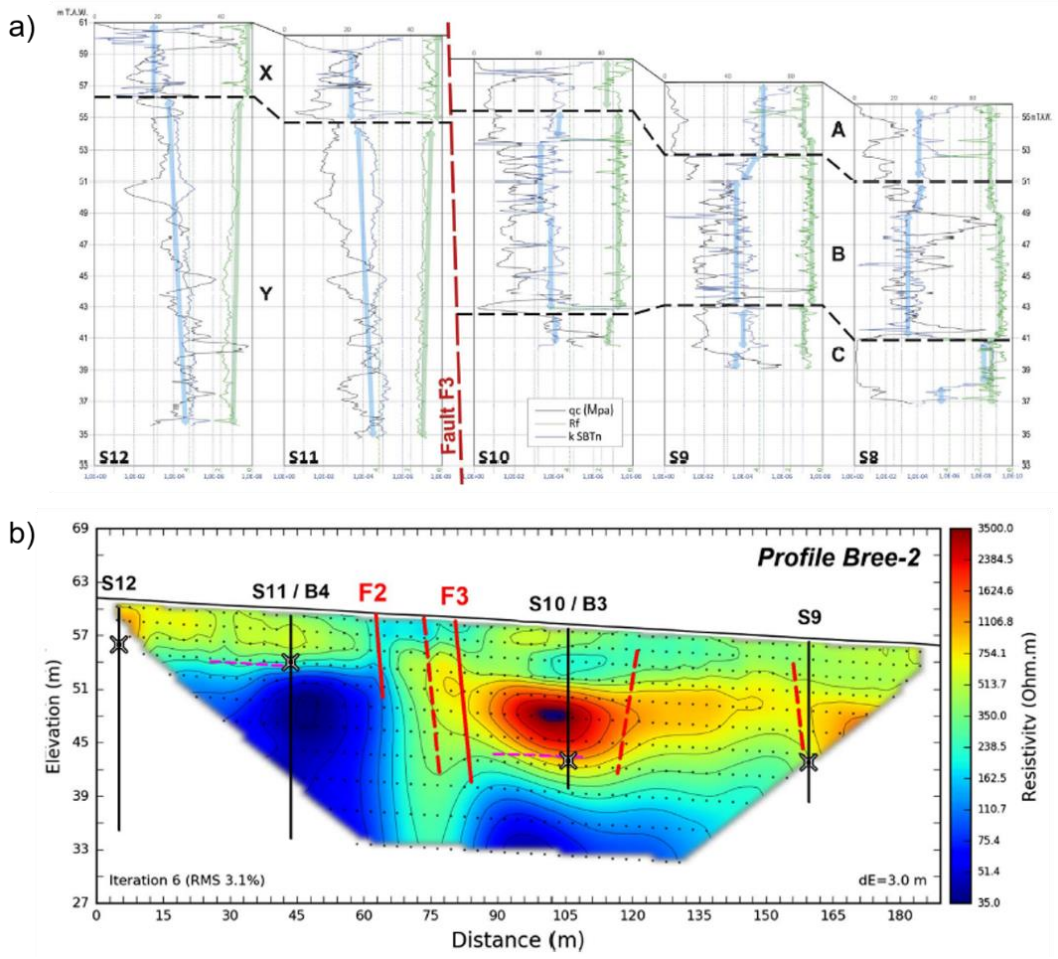

Figure 11. a) Correlation profile of the different CPTs in Bree Site. b) ERT-profile Bree-2 with the interpretation by Deckers et al. (2018) of the fault splays (F2 and F3) as well as the base of the Meuse Group (crosses and pink lines).

The groundwater table monitoring in the boreholes shows that there is a strong difference in the height between the hanging wall (+46.15 m TAW on average) and the footwall (+58.53 m TAW on average), resulting on a ~12.5 m difference on average. As both boreholes are just separated by 53.5 m, Deckers et al. (2018) interpreted the jump in the groundwater level as the result of faults F2 and F3 in between them. From the hand auger borings (Fig. 10), Deckers et al. (2018) observed two groundwater table changes: one step across F2, between HA3 and HA4, and a second step across F3, between HA5 and HA6. The second step was found to be larger than 1.3 m as the groundwater table in HA6 was not found, which according to Deckers et al. (2018) implies that most of the groundwater change is caused by the fault splay F3.

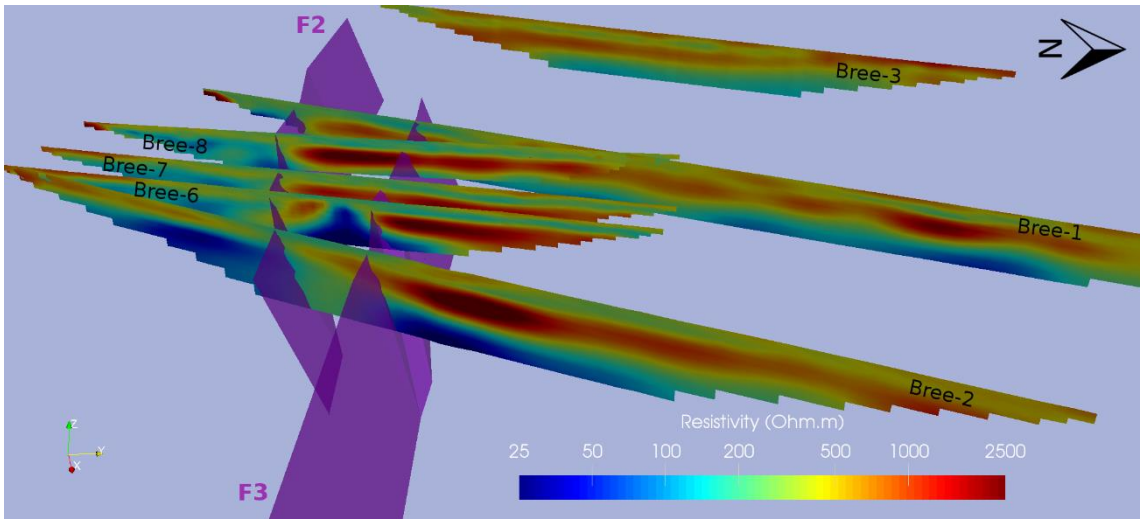

Figure 12. 3-D view of the ERT-profiles recorded by Deckers et al. (2018) at the Bree Site showing the overlap between the two fault splays (F2 and F3).

Although the site has been studied in detail, there is still some uncertainty on how both fault segments are connected (Van Noten, K., personal communication). Two possibilities are considered in this study: a soft-linked and a hard-linked fault (Fig. 13). A soft-linked fault would imply that groundwater connection between the footwall and the hangingwall is possible, while a hard-linked fault would imply no hydraulic connection between the fault walls at all. This uncertainty is expected to be resolved in this study by means of testing different scenarios in a groundwater model representing the Bree site.

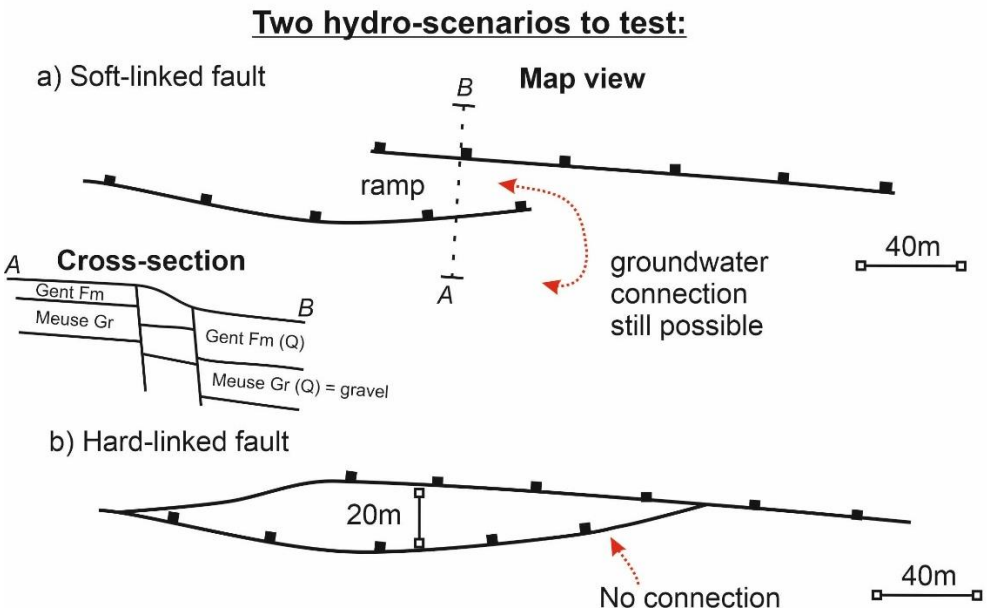

Figure 13. Conceptual drawing of the two possible hydrogeological scenarios at the Bree Site. (a) Soft-linked fault scenario with a conceptual cross section of the fault splays, and (b) hard-linked fault scenario.

3. Groundwater modelling methodology

A conceptual model has been developed based on field investigations carried by different authors (e.g. Bense et al., 2003b; Deckers et al., 2018; Lapperre et al., 2019) in the RVG, its sediments, the border faults and in the GBF. From regional data, it is known that in the Campine Basin, the flow regime has a SW-NE direction. Due to the presence of several faults, which separate the different plateaus in this area (Campine, Reppel and Bocholt), the regional hydraulic gradient is altered, causing large hydraulic head differences between those plateaus (Deckers et al., 2018). Therefore, the faults act as flow-barriers, preventing groundwater to easily flow through them. The geology of the Campine Basin consists mainly of unconsolidated sediments from the Quaternary (see section 2.2 for more detail), which compose the aquifer system in this area. For this reason, the contrast between the hydrogeological properties from the sediments and the fault is expected to be responsible for the head difference between the footwall and the hanging wall of the GBF.

3.1. Conceptual model

The conceptual model has been constructed despite a lack of detailed geological and hydrogeological information in the Campine Basin, except in the two study sites, for which detailed geological, geophysical and hydrological information is available (see sections 2.3 and 2.4). Despite this lack of information, the goal of this study is to investigate the effect of the fault properties on the hydraulic head distribution and the flow regime.

For this reasons, two different models are proposed. For the first model, a synthetic case based on the Maarlo site is proposed. The aim of this synthetic case is to assess the sensitivity of the parameters controlling the hydraulic head distribution and flow regime in a 2D numerical model, simulating a cross-section with the fault located at the centre of the model. Such a 2D model assumes that the direction of flow is perpendicular to the fault. As mentioned before, the GBF has mostly a WNW-ESE orientation, while the regional gradient has a SW-NE direction. Therefore, it is fair to assume that flow will occur orthogonally to the fault. Based on the knowledge built from the synthetic case, we calibrate a local model for the Maarlo site with the available monitoring data from piezometers in transient state. The synthetic case will thus mimic the conditions observed in Maarlo. The second model will consist on a 3D numerical model of the Bree site. There, the main interest is to assess the local effect of the type of link between the two GBF splays on groundwater flow.

Modelling choices have been made regarding the available geological and hydrogeological information at each of the sites and the goal of this study. In both models, each of the hydrogeological domains represented consisted of a homogeneous isotropic volume. This means that all the cells associated to a same hydrogeological unit are simulated as an equivalent porous medium. Moreover, a continuum approach will be used to simulate the fault damage zone in both cases. With this approach, the cells within the area that corresponds to the fault are assigned hydraulic properties different from those of the hydrogeologic units. Therefore, the fault zone is simulated as a hydrogeological unit itself. However, as the fault zone consist of a narrow area

(around 4 m wide), a refinement of the grid around it will be necessary so that the cell size is smaller than its width. The rest of the choices are independent for each of the models and thus, will be described separately for each site below.

3.1.1. Maarlo case

Modelling choices

From regional data, it is known that the flow direction is perpendicular to the fault, which in the Maarlo site is composed of a single segment. For these reasons, this case will be studied as a cross-section perpendicular to the Grote Brogel Fault. The model was built as a 3D-model but only with a single cell in the y-direction parallel to the fault. The fault was set at the centre of the model as the main feature, and the model length was set to 2 km in total. The limits of the model were thus, expanded to 1 km at each side of the fault to minimize as much as possible the effect of the boundary conditions on the simulation. There are no specific geomorphological or hydrological features (such as surface water catchment divide, surface water body, etc.) which could be used as boundary conditions in the nearby zones of the Maarlo site on which the synthetic case is based. Instead, regional piezometric information from the open source Underground Databank of Flanders (Databank Ondergrond Vlaanderen; DOV) was used to set the boundary conditions at the edges of the model (see below). In the vertical direction, the model was set to be 30 m thick, which is thought to be deep enough to minimize the effects of the chosen bottom boundary condition (no flow condition) in order to focus on the shallow hydrogeological behaviour of the fault. Both steady-state and transient-state simulations will be performed for this site.

For steady-state simulations, the imposed hydraulic heads were artificially increased by 10 m from their original value. This was done to avoid problems related with the dry cells that can occur in MODFLOW when a fine vertical discretization is used in combination with the Layer property flow package for shallow unconfined aquifers (Harbaugh, 2005). This implies that once a cell is considered dried during a simulation it cannot be wet again throughout the rest of the simulation. Depending on the choice of the initial hydraulic head, such a situation can cause convergence problems. Therefore, if the cell discretization in the vertical direction is too fine compared to the fluctuations of the groundwater table across the model, dry cell problems could arise during the simulation. For this reason, the groundwater system was simulated as a confined aquifer, which means that during a simulation it always remains fully saturated with water. Such an approach has already been used on groundwater modelling by other authors and its influence on the model outputs in steady-state is limited as no fluctuation of the water table is modelled (e.g. Bense and Person, 2006; Vandenbohede and Lebbe, 2006). This approach was chosen to allow the use of a single discretization for all tested scenarios. Indeed, the synthetic case was designed to test a broad range of parameters resulting in different water levels, which would have required an ad-hoc adaptation of the grid to each scenario. Although the number of cells in the vertical direction remained the same (30), the number of hydrogeological units varied throughout the different

scenarios, which will be defined later in this section. The computed hydraulic heads were decreased by 10 m to match the observed values.

For the transient-state scenario, the aquifer was simulated as unconfined. The topography of the area, which was interpolated from the 5m Digital Elevation Model (DEM) of Flanders (VMM, 2004), was set as the top of the model. In order to simulate the aquifer as unconfined and avoid the dry cells related problem, the first 10 m in the z-axis were considered as a single cell, so that it could accommodate the hydraulic head difference created by the fault. The rest of the cells in the vertical direction were assigned a height of 1 m.

Boundary conditions

Mathematically, boundary conditions are required to solve the partial differential equations. In MODFLOW, they are also used to include the stress packages that add terms to the flow equation representing inflows or outflows (Harbaugh, 2005). Different boundary conditions were set to the model limits for groundwater flow. The piezometric data obtained from Deckers et al. (2018) is restricted to the fault area and thus, it was not sufficient to set a realistic boundary condition at the simulated scale. For this reason, open source groundwater data DOV was used, which enabled to select piezometers in the vicinity of the site to estimate the piezometric level along the direction of the model (SSE-NNW) to set more realistic boundary conditions. A groundwater divide could not be found to impose a no flux boundary condition. However, piezometric data from the zone was available. Therefore, a hydraulic head was imposed using the CHD (Time-Variant Specified-Head) package. This package allows to set a constant head throughout the remainder of the simulation in a specified cell (Harbaugh, 2005). Piezometer 913/23/7 (DOV, 2003a) was used to impose the head in the hanging wall, while piezometer 935/23/16a (DOV, 2003b) was used for the foot wall. The hydraulic heads were interpolated linearly (eq. 4, 5 and 6) at the desired distance (1000 m for each fault block). The averaged head over the available time series for each piezometer was used to determine its values.

$$\frac{\Delta h}{L} = \frac{h_x - h_0}{x} \quad (4)$$

$$h_i = 1000 \cdot \frac{\Delta h}{L} + h_0 \quad (5)$$

$$h_i = h_0 - 1000 \cdot \frac{\Delta h}{L} \quad (6)$$

Where $\Delta h \cdot L^{-1}$ is the gradient, h_x is the hydraulic head at distance x, h_0 is the head at distance zero, and h_i is the hydraulic head at 1 km distance. Eq. 5 corresponds to the hydraulic head interpolation in the foot wall, whereas eq. 6 corresponds to the interpolation in the hanging wall. The validity of the imposed head as a boundary condition in the model will be tested by changing the foot wall boundary condition type to a zero-equivalent flow rate. Furthermore, at the lateral sides parallel to the cross-section and bottom boundaries of the model, a zero-equivalent flow rate boundary condition was imposed. The former implies that the flow direction is parallel to the orientation of the model, whereas the latter implies that there will be no water flowing upwards or downwards from the bottom of the model.

For the steady-state simulations, a constant recharge was imposed to infiltrate vertically along the model through the Recharge Package (RCH), which is designed to simulate an areal distributed recharge to the groundwater system (Harbaugh, 2005). The recharge was estimated from the precipitation data of the Kleine Brogel weather station (maintained by the Royal Meteorological Institute of Belgium) that lies 2 km NW from the Maarlo site. The precipitation data comprises a time span of 316 days between November 2015 and September 2016. In steady state, the winter period precipitation data was used, for which a recharge rate of 0.00182 m/d was calculated using a ratio of 65% of the precipitation.

For the transient-state simulations, although the RCH package was used, the recharge was not simulated as constant through the time. First, to observe the response of the model to precipitation events, different scenarios were simulated (e.g. single precipitation events). From these scenarios it was observed that the response in the hanging wall to the recharge was fast, which does not match what it is observed in the monitoring data. This is because the recharge package assumes that recharge occurs directly at the water table and therefore ignores flow processes in the unsaturated zone. Since the unsaturated zone of the hanging wall is thicker, the behaviour is different from the foot wall. The Unsaturated flow package can be used to avoid this problem, but it requires to define new parameters to calculate the relative hydraulic conductivity in the unsaturated zone. Therefore, it was decided to simulate the recharge in the footwall and the hanging wall differently. For the synthetic test, the recharge was set to happen only in the footwall, while in the hanging wall the recharge was set to be null. This allows to simulate the hydraulic response in the hanging wall to flow across the fault only. For the calibration with real data, this is not realistic as some recharge does occur in the hanging wall. It was therefore modelled, but this will be explained further in this report as it is part of the calibration process.

Distributed parameter model

Even though no field data is available to estimate the values of the different parameters, studies performed by other authors in the RVG (e.g. Bense et al., 2003b; Lapperre et al., 2019) provide a valid range of values. In addition, open source data from DOV is available regarding geological and hydrogeological parameters. To carry this study on, a range of the hydraulic conductivity for the fault and the geological formations were selected according to the reviewed literature. Lapperre et al. (2019) discuss a hydraulic conductivity range for faults from 0.001 to 32 m/d for already existing calibrated models in the RVRS, and a range from 0.013 to 22.1 m/d for *in situ* measurements. Therefore, the tested hydraulic conductivity values of the fault were comprised between these ranges. The K_x values of the geological formations were selected according to the Hydrogeological 3D-model v1.1 (H3Dv1.1; Lebbe and Vandenbohede, 2004) and the Hydrogeological Mapping (HCOVv1; Meyus et al., 2000) from the DOV. For further testing the effect of the geological formations, multiples from the selected values were used (Table 1).

Table 1. Parameters used for the sensitivity analysis. The base parameters were extracted from DOV's H3Dv1.1 (Lebbe and Vendenbohede, 2004).

K_x (m/d)	K_z (m/d)	S_y	S_s (m-1)	HCOV code	Reference
34.4	3.44	-	-	-	17.2 (x2)
17.2	2.93	0.10	3.79E-05	0230	Lebbe and Vandenbohede (2004)
6.0	0.6	0.05	3.13E-04	0100	Lebbe and Vandenbohede (2004)
3.0	0.3	-	-	-	6.0 (/2)
0.6	0.06	-	-	-	6.0 (/10)

The geometrical properties of the fault tested in the different scenarios and the hydrogeologic units (HGU) were also extracted from previous studies in the RVG. Concerning the thickness of the hydrogeologic units, the observations from the Maarlo site (Deckers et al., 2018) were taken as reference, while the geometrical properties of the fault (dip and width of the fault zone) were based on previous studies carried out by Bense et al. (2003b) and Deckers et al. (2018). Although the deformation and hydraulic properties of the GBF have not been studied in detail, Bense et al. (2003b) have studied these properties on other major faults of the RVRS, such as the Geleen Fault, which are also located in unconsolidated sediments. In this study, Bense et al. (2003b) found out that the fault core has a width of ~10 cm and it can contain a clay smear of up to 2 cm, while the damage zone can expand up to 2 m from the fault core. Therefore, the tested range of the fault zone width was between 0.2 m and 4 m, where the fault core would be placed in the centre of this zone. The dip of the GBF in the near surface study carried out by Deckers et al. (2018) at the Maarlo site is rather steep (~80º). Nevertheless, a range of dipping angles between 90º and 60º was tested. For transient state simulations, the values in Table 1 of the specific yield (Sy) and specific storage (Ss) were used for the different hydrogeological units.

Scenarios definition

Three major scenarios were defined to test the parameters controlling the groundwater flow across the GBF: a steady-state simulation with a single hydrogeological unit at each side of the fault (Fig. 14a); a steady-state simulation with two hydrogeological units (Fig. 14b); a transient-state simulation (Fig. 14c). As mentioned before, the fault was placed at the centre of the model thus, separating the foot wall from the hanging wall. Moreover, in the first two scenarios, the aquifer was simulated as confined, while in the transient-state scenario it was simulated as unconfined as it has already been mentioned.

For the first scenario (Fig. 14a), different sets of simulations were performed as a sensitivity analysis of the target parameters. Therefore, the values remained fixed or changed during a specific set of simulations. The definition of these sets of simulations can be found in detail in section 4.1.1 (Table 2). Although the parameters may change through the different sets, the hydraulic parameters of a hydrogeological unit in both walls of the fault were the same in all simulations.

For the scenario with two hydrogeological units, the geometries of the layers were simplified, and their thickness was constant through the whole model (Fig. 14b). In the footwall, the thickness of

the first HGU was 4 m, while in the hanging wall the thickness of the first HGU was 10 m. These thicknesses are a simplification of the Maarlo site borehole and CPT data from Deckers et al. (2018) study. The top HGU corresponds to the Meuse Gr. and the used hydraulic values were those from the H3Dv1.1 (HCOV code 0100; Table 1). The same applied for the bottom HGU, using the hydraulic properties with the code 0230 from HCOV (Table 1).

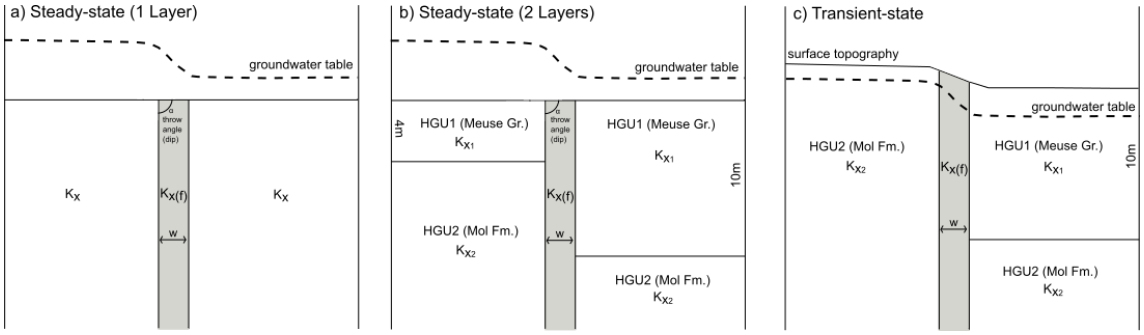

Figure 14. Schematic representation of the different major scenarios tested in the synthetic model. The HGUs values do not change from the footwall to the hanging wall. a) Layout for the sensitivity analysis of the different parameters. b) Two-layer scenario inspired on the Maarlo site. c) Transient-state layout, where the aquifer is simulated as unconfined.

For the transient-state scenario, the outline of the model remained the same, with a single HGU in the foot wall and two HGUs in the hanging wall (Fig. 14c). This simplification was done because the first layer of the model was larger than the thickness of the HGU corresponding to the Meuse Gr., which is the top geological layer in the area. In the hanging wall however, it was possible to represent both HGUs with a simplified geometry. The HGU corresponding to the Meuse Gr. was assigned the hydraulic properties of HCOV code 0100, while those corresponding to the Mol Fm. were assigned the ones of HCOV code 0230.

3.1.2. Bree case

Modelling choices

For this model, geological units were simplified and grouped by hydrogeological units (HGU), consisting respectively of the Gent Fm and the Meuse Gr for the first HGU, and the Mol Fm for the second HGU. The thickness of this HGUs throughout the extents of the model was extracted from DOV by means of the virtual boring tool (available at: https://www.dov.vlaanderen.be/) at specific points. Later, the geological contact between the HGUs was extrapolated from borehole data, including the CPTs and the boreholes from Deckers et al. (2018) study to the extent of the model, and creating thus a 3D model of the HGUs. This step enabled the interpolation of the HGUs into the grid with a more realistic geometry. To simplify the complex stratigraphy and avoid dry cell problems, 3 layers were used. The boundaries of the model were set as far as possible from the Bree Site location to minimize the effect of the boundary conditions on the result, while keeping it restricted to a local scale (Fig. 15). In addition, a steady-state simulation was chosen to test the different fault-linking scenarios. The fault was not represented with the Flow Barrier Package from MODFLOW but explicitly with polygons, assigning a hydraulic conductivity to the

area covered by those polygons. The Bocholt fault was set as the northern limit of the model (Fig. 15). However, it will not be simulated as a no flow boundary condition, but as an imposed hydraulic head. This will be discussed later in this report. Even though the Reppel fault intersects with the GBF inside the limits of the model, at its western edge, it was not considered in this study as there is no hydrogeological data available. The boreholes and the CPT's locations were used as observation points. Moreover, an additional virtual observation point was placed in between both segments to record better the response in each of the scenarios.

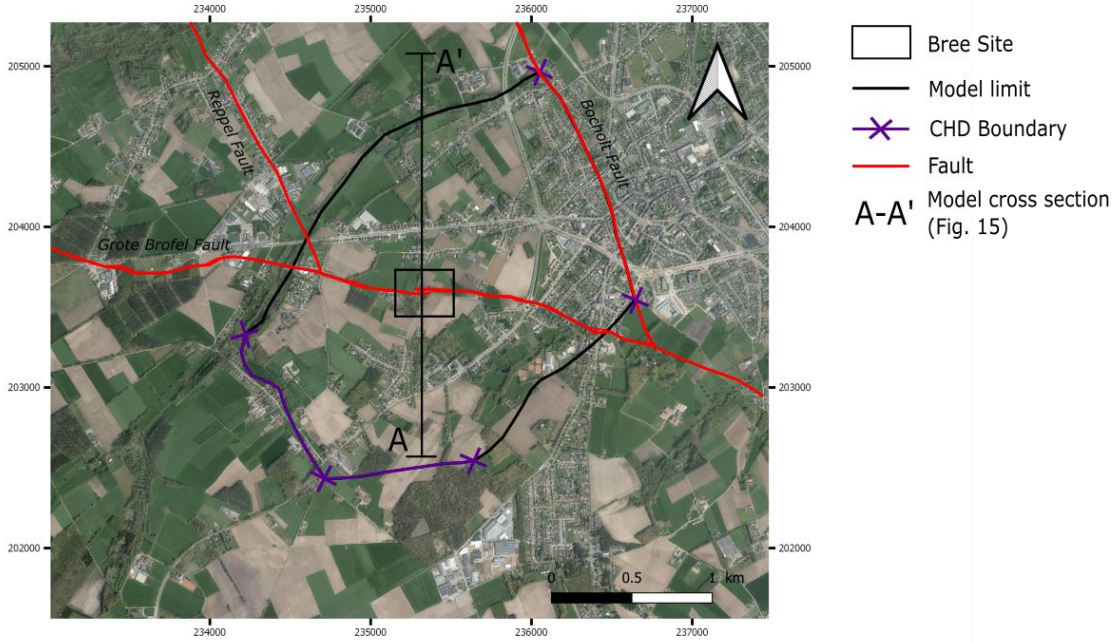

Figure 15. Extension of the Bree 3-D numerical model, with the faults and the boundary conditions displayed. For cross section A-A' see Fig. 15. Coordinates in Belgian Lambert 1972.

Boundary conditions

The southern and north-eastern limits of the model were assigned a specified head with the CHD package (Fig. 15). The imposed heads on those limits were set regarding the available regional piezometric data and using the equations 4, 5 and 6 to interpolate the hydraulic head to the desired distance. For the north-western and south-eastern limits, the two creeks close to the Bree site were selected. Although the river package (RIV) could have been used for both limits, the chosen boundary condition was a no flow boundary, assuming that the creeks are draining the aquifer from both sides and is therefore where the lowest water table of this area occurs. Tests with the river package as boundary conditions showed that it has almost no effect on the distribution of the hydraulic head. As only steady-state simulations will be used for the different scenarios, a yearly average recharge was calculated. It is known that the recharge in Flanders occurs mostly in winter, and that the average infiltration is 219 mm/year (Meyus et al., 2004). From this value, a recharge rate of 0.0007 m/d was obtained. Contrary to the Maarlo case, the recharge occurred homogeneously throughout the whole extension of the model.

Distributed parameter model

Despite the lack of field hydrogeological data in the area, the different parameters were assigned its values based on the tests and calibration performed on the Maarlo case. Out of the three layers of the model (Fig. 15 and 16), the first one corresponds to the Gent Fm and Meuse Gr HGU and was assigned the hydraulic values of HCOV code 0100 (Table 1). While the second and third layers were assigned the values of HCOV code 0230 (Table 1) and correspond to the Mol Fm HGU (Fig. 16). The fault damage zone was represented as a polygon following the trace defined by Deckers et al. (2018). The width of the damage zone was set to ~3 m as inferred from the Maarlo's case calibration, and its hydraulic conductivity was assigned a value of 0.012 m/d. Although the GBF in Bree presents a gentler dip (~60º) than in Maarlo (~80º; Deckers et al., 2018), it was represented as vertical to simplify the discretization. The vertical component of the hydraulic conductivity (K_z) was set to be 10 times lower than the K_x for the fault, while for the HGUs, the values from the H3Dv1.1 (Table 1; Lebbe and Vandenbohede, 2004) were used.

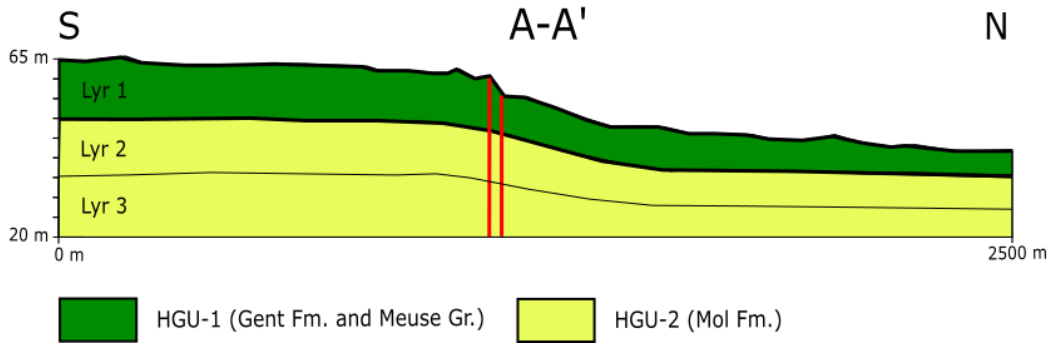

Figure 16. Schematic representation of the Bree 3-D numerical model. 3 Layers where used to simplify the stratigraphy. The position of the fault splays (red lines) is shown. Both fault splays were considered as vertical for modelling purposes. The parameter distribution is subject to the HGU of each layer.

Scenario definition

As mentioned before, how the segments of the GBF link with each other is still unknown. For this reason, four different scenarios (Fig. 13) will be considered: a scenario without fault (1) to simulate the regional groundwater flow; a scenario with a soft link (2), which means that there is no connection between the segments; a scenario with a hard link on the eastern part (3); and a scenario with a hard link on both sides (4).

3.2. Mathematical and numerical model

The three-dimensional movement of groundwater with constant density through porous material may be described by the following partial-differential equation (Eq. 7; Harbaugh, 2005):

$$\frac{\partial}{\partial x} \cdot \left(Kx \cdot \frac{\partial h}{\partial x}\right) + \left(Ky \cdot \frac{\partial h}{\partial y}\right) + \left(Kz \cdot \frac{\partial h}{\partial z}\right) + W = S_s \cdot \frac{\partial h}{\partial t} \qquad (7)$$

Where K_x, K_y and K_z are the hydraulic conductivity in the x, y and z coordinates (L/T); h is the hydraulic head (L); W is a volumetric flux per unit volume representing sources and/or sinks (1/T);

S_s is the specific storage (1/L); and t is time (T). Equation 7 together with specification of flow and/or head conditions at the boundaries of the system and specification of initial-head conditions, constitutes a mathematical representation of a groundwater flow system (Harbaugh, 2005).

The groundwater flow equation (Eq. 7) becomes steady state when the specific storage term (left hand side) is zero. The resulting equation specifies that the sum of all inflows and outflows, from adjacent cells and external stresses, is zero for each cell in the model and therefore, it only requires a single solution of the simultaneous equations (Harbaugh, 2005). The objective of transient-state simulations is to predict the head distribution at different successive moments in time, given the initial head distribution, the boundary conditions, the hydraulic parameters and the sources and sinks (Harbaugh, 2005). This type of simulation requires multiple solutions for multiple time steps as the set of finite-difference equations is reformulated at each time step, where a new system of equations must be solved (Harbaugh, 2005). Note that for solving the flow in unconfined aquifers, the flow along the water table is simplified to 2D horizontal flow. The specific yield must be considered in the storage term to account for the variation of the water table.

To solve the flow equation, the finite-difference groundwater model code MODFLOW-2005 is used in this study. The finite-difference approach approximates the partial-derivative equations using a finite number of discretized algebraic equation, with the hydraulic head in each cell of the model as unknowns. It results in a linear system of equations with as many equations as there are cells in the model. It uses an iterative approach to solve the system. In transient state, the time-derivative is solved using an implicit approach, ensuring unconditional stability. We refer to McDonald and Harbaugh (1988) and Harbaugh (2005) for the details on the numerical implementation. The chosen graphic interface was GMS (Groundwater Modeling System; Aquaveo, 2018), which allows an easy conceptual model approach as well as the representation and interpolation of GIS and stratigraphic data into a MODFLOW grid.

3.3. Grid construction

All numerical models use a grid framework, where hydrogeological data is imported and interpolated into the grid (Singhal and Gupta, 2010). The gridding process subdivides the space into discrete blocks, in which the system of equations is solved. The grid approach for each of the models is completely different and therefore, they will be discussed separately.

As it has already been mentioned, the Maarlo site will be studied as a cross-section because most of the groundwater flow in this zone occurs orthogonally to the fault. For this site, the length of the constructed models was set to be 2 km. The synthetic model used to test the sensitivity of the parameters consisted on 600 cells in the x-direction, a single cell in the y-direction and 30 cells in the z-direction, each of which had a thickness of 1 m. The zone around the location of the fault and the monitoring piezometers was refined due to its interest for this study. GMS offers the opportunity to generate a refined grid automatically around refining points. This option was used setting a base cell size of 0.2 m, an increment factor of 1.2 and a maximum cell size of 2 m. In order to calibrate the real data, a new grid was constructed. For this model, georeferencing was

used to interpolate the DEM elevation into the grid, so that its top represented the elevation, which could have an influence on the head distribution. For the grid to be perpendicular to the fault, which presents an NNW-SSE trend, a rotation angle of -35º in the x-y plane was applied. The grid of this model was composed of 10170 cells, 340 cells in the y-direction, 30 cells in the z-direction and a single cell in the y-direction. The automatic refinement was also used in this case, setting a base cell size of 0.2 m, a bias of 1.2 and a maximum cell size of 20 m.

The grid size of the Bree site is determined by its boundaries and the refinement of the area of interest, where the two splays of the GBF link. As it has been done for the Maarlo site, the model was georeferenced and the elevation data from the 5m DEM of Flanders (VMM, 2004) was used to set the top of the model. In addition, no rotation angle was applied to the grid in any of the planes. The extension of the model was set to be 2486 x 2518 m, and a thickness of 50 m on the z-direction. The grid was composed by a total number of 100.000 cells. However, only the cells which were inside the boundaries of the model were set as active. This led to a total of 84500 active cells, with 164 cells in the x-direction, 200 cells in the y-direction and 3-cells in the z-direction. The thickness of the z-direction cells was defined by the interpolation of stratigraphic data from virtual and site boreholes into the MODFLOW grid. For the refinement of the grid, the base cell size was set to 1 m, the bias to 1.2 and the maximum cell size to 50 m.

4. Results and discussion

4.1. Synthetic case

The goal of the synthetic case was to perform a sensitivity analysis on the parameters that may control the hydrogeological behaviour of the fault zone. Such parameters are the hydraulic conductivity, the width of the fault zone and the dip of the fault. Different scenarios, where some of these parameters remained fixed and others were variable, were performed to assess which of them has a more significant impact. As explained in section 3, a single-layer model was used for this purpose. Few tests were also performed in a two-layer model. Using the Maarlo data, the model was calibrated.

4.1.1. One-layer model

Hydraulic conductivity

In order to test the sensitivity of the hydraulic conductivity (K_x), of both the geological formation and the fault damage zone in the model, different scenarios were simulated fixing either one of the values or the other. The geometric properties of the fault remained fixed for the sensitivity analysis of the hydraulic conductivity to reduce to the minimum its influence on the result. These scenarios are summarized in Table 2. As mentioned before, the computed hydraulic head have been decreased by 10 m to match the observed data in Maarlo.

Table 2. Summary of the different scenarios simulated to test the hydraulic conductivity of the geological formation and the fault damage zone.

Scenarios		Sensitive parameters			
		Formation K_x (m/d)	Fault K_x (m/d)	Fault zone width (m)	Fault dip (º)
A	A1	0.6	Fixed	Fixed at 4 m	Fixed at 90º
	A2	3.0			
	A3	6.0			
	A4	17.2			
	A5	34.4			
B	B1	Fixed	0.005	Fixed at 4 m	Fixed at 90º
	B2		0.02		
	B3		0.08		
	B4		0.32		
	B5		1.28		
	B6		5.12		
	B7		20.48		

The hydraulic gradient was calculated from the hydraulic head distribution for the three sections in each scenario (further noted as Sc.). These sections are the footwall, the fault damage zone and the hanging wall. In addition, the gradient in the near-fault zone, where the effect of the boundary condition is less important, was also calculated for the footwall and the hanging wall from the edge of the damage zone to a distance of ~30 m in each of the fault blocks.

Footwall

In the footwall, when the fault K_x remains fixed (Sc. A, Table 2), the calculated gradient increases when the formation K_x decreases (Fig. 17a). Although these gradients do not fully represent the obtained hydraulic head distribution in the footwall, they show that the model is more sensitive to lower formation's K_x as the variation in the gradient between a formation K_x of 3.0 m/d (Sc. A2) and 6.0 m/d (Sc. A3) is much greater than between 17.2 m/d (Sc. A4) and 34.4 m/d (Sc. A5). In addition, with a fixed formation K_x (Sc. B), for lower fault hydraulic conductivities, the simulated head distribution presents a maximum in its parabolic shape, which implies the presence of a water divide in the footwall (Fig. 17b). This an indirect consequence of the fixed head boundary and recharge conditions. Nevertheless, there is a threshold fault K_x after which, the parabolic distribution is not observed anymore (Fig. 17b). These threshold values have only been observed through simulations in which large formation K_x values (those from Sc. A4 and A5) were fixed. This can also be observed in the calculated gradients (Table 3), in which after the fault's K_x threshold is overcome, the gradient changes its sign from positive to negative, showing a decrease of the hydraulic head over distance in the footwall from that point on. For formation K_x values equal or lower than 6.0 m/d, the maximum in the footwall's parabolic shape is observed independently of the fault's hydraulic conductivity. Nevertheless, the calculated near-fault gradient in the footwall does not show any maximum as its sign remains always negative (Table 3), which

implies that groundwater flows towards the fault. This near-fault gradient is more sensitive to low hydraulic conductivity values of both parameters (fault and formation K_x) as well.

Table 3. Calculated gradient for Scenarios A and B combined. FW: footwall; HW: hanging wall.

Formation K_x (m/d)	Sector	Gradient (Δh/L) per Fault K_x (m/d)						
		0.005	**0.02**	**0.08**	**0.32**	**1.28**	**5.12**	**20.48**
34.4	Footwall	0.0006	-0.0001	-0.0014	-0.0026	-0.0031	-0.0033	-0.0033
	Fault	-2.0546	-1.6953	-0.9985	-0.3779	-0.1085	-0.0282	-0.0071
	Hanging wall	-0.0012	-0.0019	-0.0032	-0.0044	-0.0049	-0.0050	-0.0051
17.2	Footwall	0.0012	0.0002	-0.0012	-0.0021	-0.0024	-0.0024	-0.0025
	Near-fault FW	-0.0005	-0.0015	-0.0029	-0.0038	-0.0040	-0.0041	-0.0042
	Fault	-1.9178	-1.3745	-0.6450	-0.2066	-0.0556	-0.0142	-0.0035
	Near-fault HW	-0.0006	-0.0017	-0.0031	-0.0039	-0.0042	-0.0043	-0.0043
	Hanging wall	-0.0023	-0.0033	-0.0047	-0.0056	-0.0059	-0.0059	-0.0060
6	Footwall	0.0037	0.0024	0.0013	0.0010	0.0009	-	0.0008
	Near-fault FW	-0.0106	-0.0087	-0.0056	-0.0045	-0.0041	-	-0.0042
	Fault	-1.5341	-0.8047	-0.2773	-0.0768	-0.0197	-	-0.0012
	Near-fault HW	-0.0015	-0.0029	-0.0039	-0.0043	-0.0044	-	-0.0044
	Hanging wall	-0.0063	-0.0077	-0.0087	-0.0091	-0.0092	-	-0.0092
3	Footwall	0.0081	0.0068	0.0061	0.0059	0.0059	-	0.0059
	Fault	-1.1743	-0.4909	-0.1475	-0.0390	-0.0097	-	-0.0006
	Hanging wall	-0.0120	-0.0133	-0.0140	-0.0142	-0.0142	-	-0.0142
0.6	Footwall	0.0470	-	-	-	-	-	0.0461
	Fault	-0.3966	-	-	-	-	-	-0.0001
	Hanging wall	-0.0536	-	-	-	-	-	-0.0543

Fault

Across the fault damage zone, when the fault K_x remains fixed, the gradient decreases as the formation K_x decreases (Sc. A). Therefore, larger formation hydraulic conductivities show steeper gradients across the fault zone (Fig. 17c). While a larger formation K_x generates steeper gradients in the simulation, larger K_x values within the fault damage zone (Sc. B) result in the generation of gentler gradients across it (Fig. 17d). This is probably related to the ratio between the formation K and the fault K, which will be discussed later. A lower hydraulic gradient across the fault zone implies that the head difference between the footwall and the hanging wall is reduced. The model has proved to be more sensitive to low fault K_x and low formation K_x values rather than to high K_x values of these parameters. Hydraulic conductivities larger than 1.28 m/d within the fault zone do not reflect a significant change in the hydraulic head distribution across the model.

The vertical hydraulic conductivity (K_z) of the fault was also tested to assess the model sensitivity to this parameter. However, the results of the different simulations showed that the model is not sensitive to the fault's K_z as the maximum variation in the hydraulic head distribution across the model was only 1 cm. This variation in the hydraulic head is not significant as the head difference between the footwall and the hanging wall on the Maarlo site, from which the synthetic model is inspired, is documented to be of a metric order of magnitude (~6 m; Deckers et al., 2018).

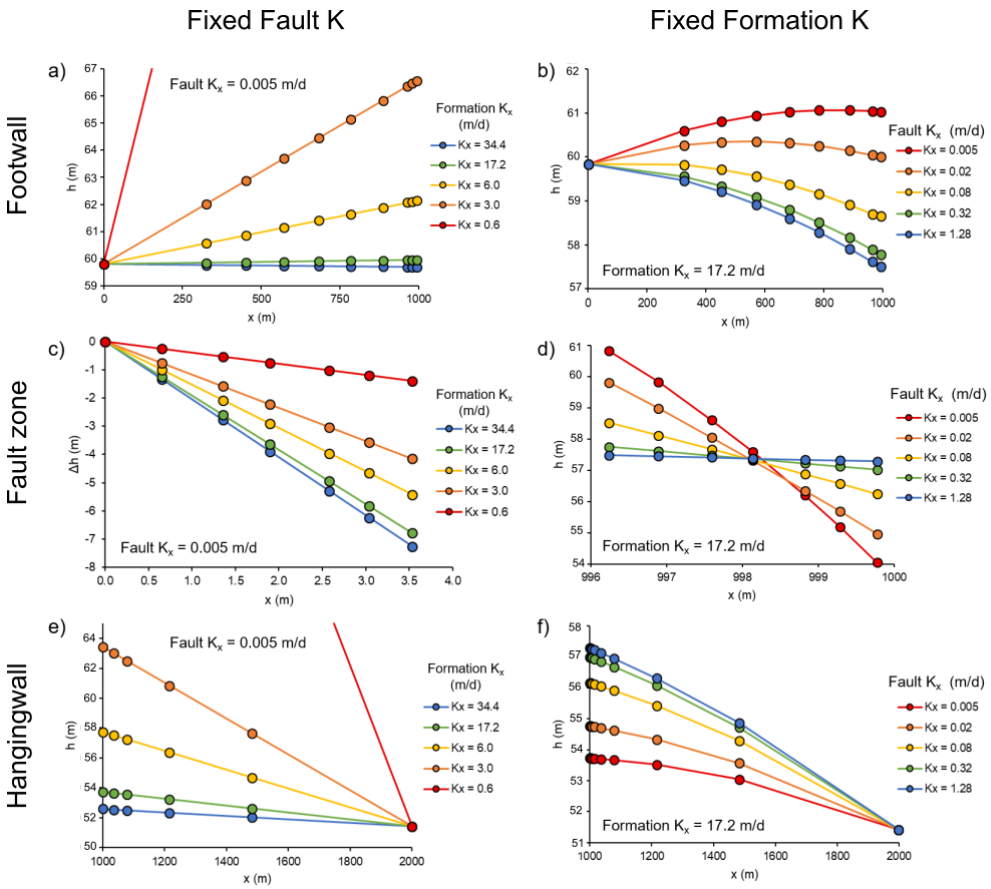

Figure 17. Plot of the calculated gradients from Sc. A (fixed fault K_x) for the footwall (a), fault zone (c) and hanging wall (e) sectors, and hydraulic head distribution from Sc. B (fixed formation K_x) for the footwall (b), fault zone (d) and hanging wall (f) sectors. The plot of (c) corresponds to the decrease of hydraulic head (Δh) along its thickness (4 m).

Hanging wall

The hydraulic gradient in the hanging wall shows a similar response independently of the tested formation and fault hydraulic conductivities. The calculated gradients are steeper for low formation K_x values (Fig. R1e) and, like in the footwall and across the fault damage zone, the model is more sensitive to these lower K_x values. Inversely to what has been observed with the formation's K_x, higher fault K_x values turn into steeper hydraulic gradients in the hanging wall (Fig. R1f) as a lower head difference, due to a gentler hydraulic gradient across the fault, must be compensated to meet the boundary condition. The near-fault gradient in the hanging wall does not reflect any significant changes (Table R2). The hanging wall's hydraulic gradient, near-fault gradient and head distribution are more sensitive to lower formation and fault zone K_x values.

Fault's geometrical properties

The geometrical properties of the fault have been tested by means of fault width and fault dip variations. For testing the geometrical properties, the fault's K_x was set to 0.04 m/d. First, the influence of fault damage zone width variations on the hydraulic conductivity was tested by changing the fault damage zone width between 4 and 0.2 m, with a fixed fault dip of 90º (Sc. C, Table 4). The influence of fault dip changes on the hydraulic conductivity was tested by fixing the

fault width at 4 m (Sc. D). Finally, the dip of the fault was tested by changing the fault width for each of the tested dip angles, which are comprised between 90º and 60º (Sc. E). In order to test better the effect of the dip, additional observation points were placed in the refined area of the model and its surroundings.

Table 4. Summary of the scenarios simulated to test the geometrical properties of the fault damage zone.

Scenarios		Sensitive parameters			
		Formation Kx (m/d)	Fault Kx (m/d)	Fault zone width (m)	Fault dip (º)
C	C1	Fixed	Fixed	4.0	Fixed at 90º
	C2			3.0	
	C3			2.0	
	C4			1.0	
	C5			0.7	
	C6			0.2	
D	D1	Fixed	Fixed	Fixed at 4 m	90
	D2				80
	D3				70
	D4				60
E	E1	Fixed	Fixed	4.0	80-70-60
	E2			1.0	80-70-60

The width of the fault's damage zone has a higher impact on the absolute hydraulic head difference between the footwall and the hanging wall rather than on the hydraulic gradient across the fault (i.e., the slope). As the fault width decreases, so does the head difference between the two walls of the fault (Fig. 18a). For a damage zone width of 4 m, the head difference between the footwall and the hanging wall is 3.92 m; for a width of 1 m, the head difference becomes 1.71 m; and, for a width of 0.2 m, the head difference between the two blocks of the fault is reduced to 0.35 m. The decrease in the head difference has an impact on the hydraulic gradient of both, the footwall and the hanging wall. The hydraulic gradient across the fault varies from -1.433 (Sc. C4) to -0.778 (Sc. C6). The general gradient in each of the fault blocks increases as the width of the fault zone decreases. However, in the near-fault zone it remains similar (Table 5).

Unlike the width of the damage zone, the fault dip has a significant effect on both the hydraulic gradient and the head difference between the two fault walls. The head difference is inversely proportional to the dip of the fault, which means that a gentler dipping fault will generate a higher head difference between the footwall and the hanging wall. Nevertheless, the increase in head difference is not linear as the dip decreases. The highest jump in hydraulic head difference is observed between a vertically dipping fault and a fault dipping 80º, where the head difference between the two walls goes from 3.65 m for a vertically dipping fault, to 5.83 m for an 80º dipping fault (Fig. 18b). With gentler dipping faults, the head difference increase is not so abrupt as it rises to 6.48 m for a 70º dipping fault, and to 7.2 m for a 60º dipping fault. The hydraulic gradient across

the fault, contrary to the head difference, it decreases as the dip of the fault becomes gentler and therefore, a 60º dipping fault will have a lower hydraulic gradient across it than a more vertically dipping fault. Nevertheless, its shape is significantly affected as it can be observed in Figure R2b. As the dip of the fault becomes gentler, the head distribution spreads further from the fault zone and into the hanging wall.

Table 5. Hydraulic gradients calculated for Scenarios C and D. FW: footwall; HW: hanging wall.

Scenario	Sector	Fault zone width (m)			
		0.2	**1**	**2**	**4**
C	Near-fault FW	-0.0040	-0.0033	-0.0029	-0.0022
	Fault zone	-0.7776	-1.4331	-1.2942	-0.9772
	Near-fault HW	-0.0041	-0.0034	-0.0031	-0.0023
Scenario	**Sector**	**Fault dip (º)**			
		60	**70**	**80**	**90**
D	Near-fault FW	-0.000583812	-0.000895637	-0.001227791	-0.002316567
	Fault zone	-0.290208701	-0.406849884	-0.544367449	-0.864646606
	Near-fault HW	-0.009063336	-0.001072577	-0.001393242	-0.002464257

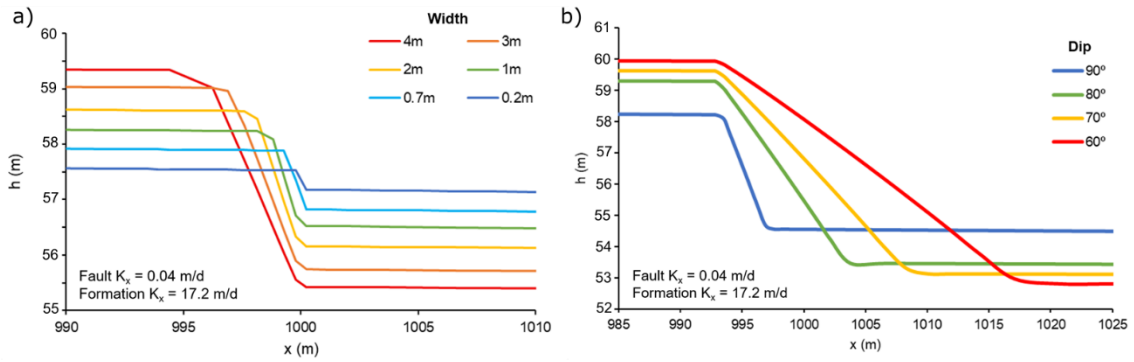

Figure 18. Hydraulic head distribution across the fault and the immediate surroundings for the different tested widths (a) of the fault damage zone and its dipping angle (b).

When the dip and the width of the fault are tested together, it can be observed that the model is more sensitive to fault dip changes than to damage zone width changes (Fig. 19). However, variations in the width of the fault zone have a higher impact on strongly dipping faults (90º and 80º) than on gently dipping faults (70º and 60º). This impact is reflected on the head difference between the footwall and the hanging wall, which is smaller for narrower fault damage zones. Taking an 80º dipping fault as an example, the observed reduction in the head difference between the two walls, from a 4-meter-wide fault zone to a 1-meter-wide fault zone simulation, is greater than for a 70º or a 60º dipping fault (Fig. 19). For gentler dipping faults thus, the head difference reduction is not as significant. Nevertheless, the slope of the hydraulic gradient across them is affected by changes in the width of the fault zone, becoming steeper (Table 5) and spreading less the head distribution into the hanging wall.

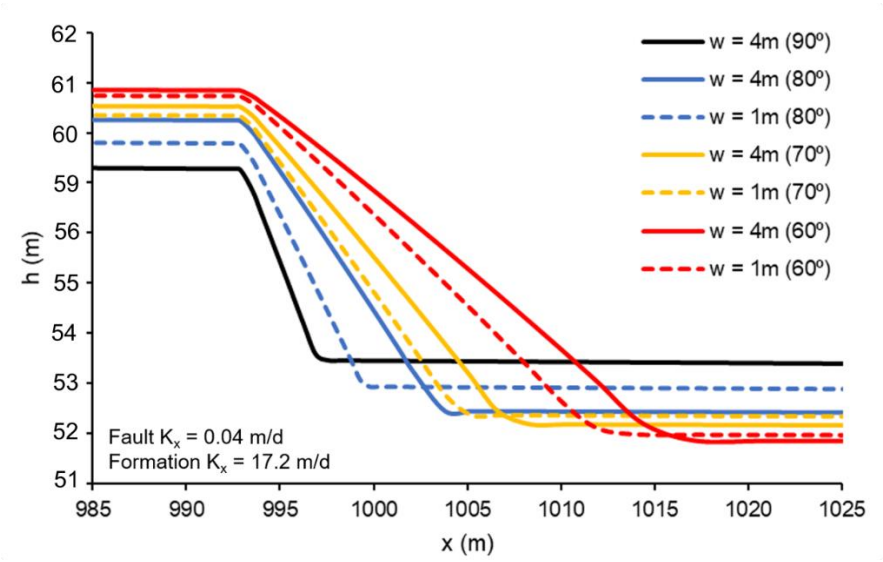

Figure 19. Hydraulic head distribution, across the fault and its surroundings, due to the effect of the fault zone width coupled with the effect of the dipping angle. Full lines show the head distribution for a fault zone width of 4 m, while dashed lines reflect the head distribution for a fault zone width of 1 m. Different colours represent different fault dips.

4.1.2. Two-layer model

A two-layer model was implemented to test the influence of heterogeneity in the surroundings of the fault zone. This model is based on the Maarlo site, which has been described in detail in section 2.3. The presence of lower hydraulic conductivity geologic formations (Meuse Gr.), on top of more conductive formations (Mol Fm.), makes the hydraulic head rise in both fault walls compared with the hydraulic head cases studied in the one-layer model simulation (Fig. 20a). This rise is larger in the hanging wall, where the Meuse Gr. is thicker than in the footwall. The effect on the hydraulic gradient across the fault, while testing the sensitivity of the hydraulic conductivity of the fault, is similar to the one observed in a one-layer model. Low hydraulic conductivity faults present steeper gradients and larger head differences between the hanging wall and the footwall (Fig. 20a). The effect of the width of the fault damage zone was also tested in the two-layer model. The behaviour observed in the two-layer model is similar to the observed in the one-layer model (Fig. 20b).

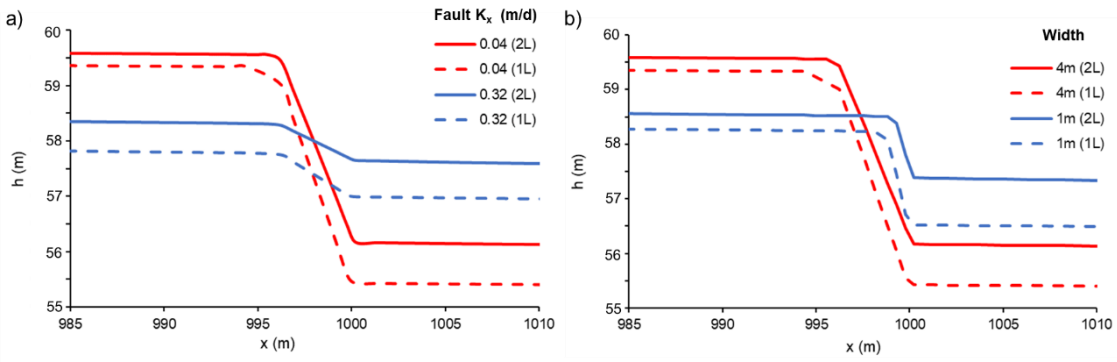

Figure 20. Comparison of the hydraulic head distribution in a two-layer (2L) and a one-layer (1L) model for sensitivity of the fault Kx (a) and the width of the fault zone (b).

Velocity vectors were generated in GMS from MODFLOW's cell-to-cell file (CCF). Those vectors are calculated based on the 2D distribution of hydraulic head to deduce the Darcy's flux amplitude and orientation. In contrast with a single-layer model, where no vertical flow could be observed (Fig. 21a), in the two-layer model vertical flow was observed (Fig. 21b). The observed vertical flow is restricted to a few tens of meters around the fault damage zone. While in the footwall an upwards vertical flow is observed, in the hanging wall the observed vertical flow shows a downwards direction. The velocity of the flow increases close to the fault zone is reduced. In the fault zone however, the flow velocity remains constant without any vertical component.

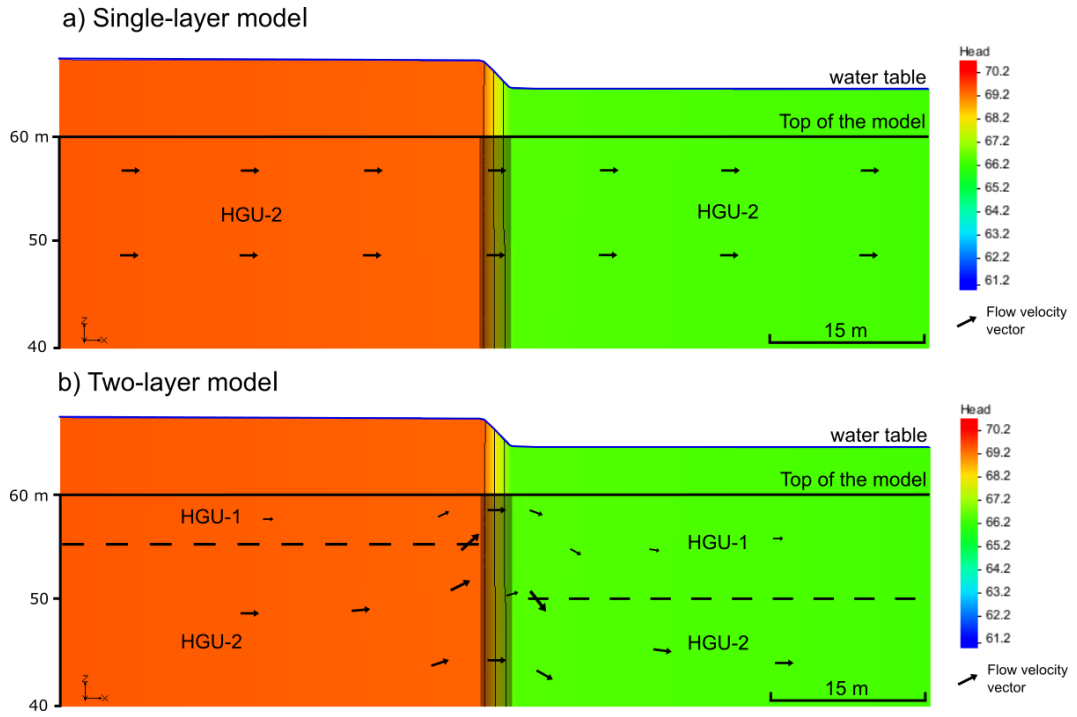

Figure 21. Cross section of the model in the near-fault zone with the flow velocity vectors displayed for a single-layer model (a) and a two-layer model (b). The length of the vector represents its magnitude.

4.1.3. Transient state

Transient state simulations were carried in order to assess the effect of the precipitation patterns through infiltration on the hydraulic head on both blocks of the fault by means of the hydraulic head difference (Δh). Three major scenarios were tested: a single precipitation event (Sc. F), a full time series with a monthly averaged infiltration (Sc. G), and a short time series with a realistic precipitation pattern (Sc. H). In each of these scenarios, different parameters of the model were tested by changing its value, to have a better insight of how the model would respond to these changes in specific parameters. All the different scenarios are summarized in Table 6.

To test a single strong precipitation event, a recharge rate of 0.08 m/d (Sc. F1) was set between the second and third time steps out of 126, with each time step representing a day. The response time to this single precipitation event is faster in the footwall, being almost immediately reflected, as expected, while in the hanging wall the response is slower as it comes from flow through the

fault only (Fig. 22). The Δh created due to the infiltration of the precipitation is much larger in the footwall than in the hanging wall. The maximum head difference in the footwall is reached earlier than in the hanging wall as it occurs approximately at time step 4, just within a day and a half after the precipitation event. In the hanging wall however, the maximum is difficult to locate as it is more sustained over time, occurring approximately around time step 20 (Fig. 22a). Although the decrease of the hydraulic head is faster in the footwall, after a period of 126 days, the hydraulic head has not yet recovered its initial values in neither of the fault blocks.

Table 6. Summary of the scenarios simulated in transient state.

Description	Scenarios		Fixed parameters	Tested parameter
Single precipitation event	F	F1	Formation Kx Fault parameters RCH	-
		F2	Formation Kx Fault parameters	RCH
		F3	Formation Kx Fault dip and width RCH	Fault Kx
Averaged RCH in a large time series	G	-	Formation Kx Fault parameters	RCH
Short time series	H	-	Formation Kx Fault parameters	RCH

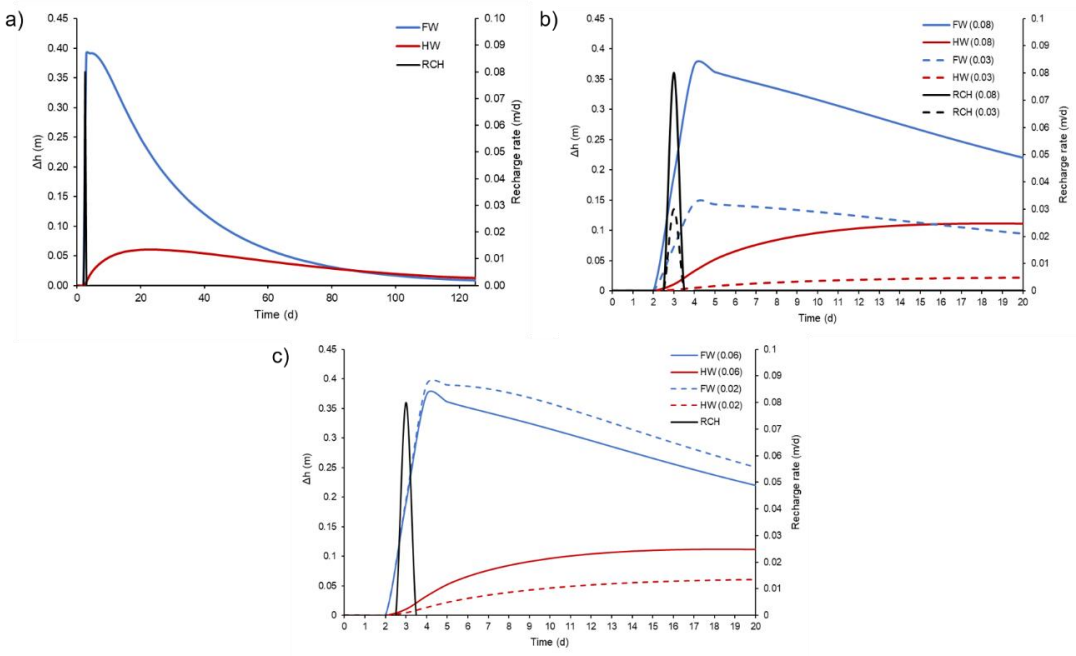

Figure 22. Computed hydraulic head difference (Δh) for single precipitation event scenarios F1 (a), F2 (b) and F3 (c). In between brackets in (b), the recharge rate in m/d. In between brackets in (c), the fault K_x in m/d. FW: footwall; HW: hanging wall; RCH: recharge rate.

The intensity of the precipitation (and subsequently, the amount of infiltrated water) and the effect of the K_x of the fault damage zone were also tested by means of a single precipitation event (Sc. F2 and F3). As expected, a less intense precipitation event (with a recharge rate of 0.03 m/d) creates a lower response on the hydraulic head, increasing the response time, reducing the maximum head difference and slightly delaying its peak in time (Fig. 22b). The hydraulic conductivity of the fault zone has an impact on the head difference of both fault blocks. With lower fault K_x values, the maximum head difference in the footwall increases while in the hanging wall it is reduced (Fig. 22c), thus significantly increasing the hydraulic gradient across the fault after a precipitation event. With higher fault K_x values, the effect is the contrary as the maximum head difference in the footwall is reduced, while in the hanging wall increases. This would imply that there is a certain flow of groundwater from the footwall to the hanging wall through the fault as already suggested by Deckers et al. (2018). Therefore, the hydraulic conductivity of the fault might control the amount of water that flows into the hanging wall from the footwall and the evolution of the hydraulic gradient with time. Note that those scenarios do not consider recharge occurring directly in the hanging wall.

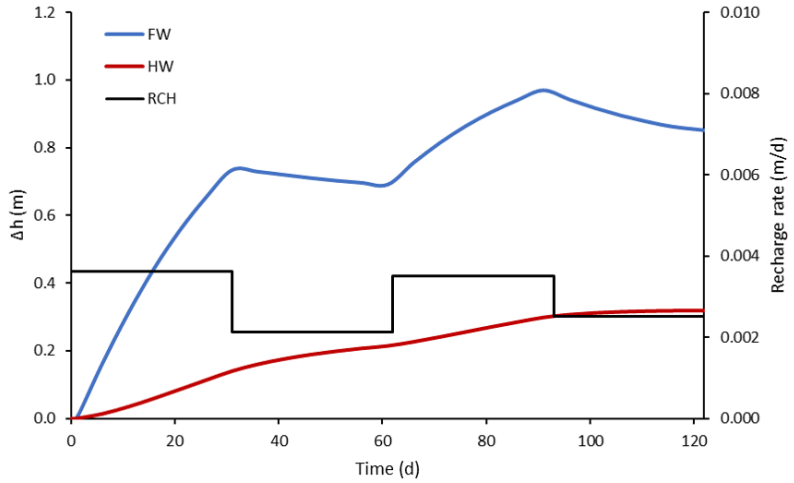

Figure 23. Computed hydraulic head difference (Δh) for a 123-day time series with an average recharge rate per month (Sc. G). FW: footwall; HW: hanging wall; RCH: recharge rate.

For Scenario G, a full time series, comprising 4 months, was simulated by averaging the recharge rate from the precipitation data throughout every month. Therefore, the recharge rate for each of the simulated months was different. During the first month the hydraulic head increases in both blocks of the fault linearly. However, in the footwall the effect is larger, reaching a maximum head difference (Δh) of about 0.8 m with respect to the start of the simulation, while in the hanging wall the hydraulic head increases around 0.15 m (Fig. 23). The second month is characterized by a lower recharge rate. Through this month, the trend of the hydraulic head is different in each of the fault blocks. While in the footwall the hydraulic head decreases with time, in the hanging wall the hydraulic head increases. Although in the hanging wall, the hydraulic head is still increasing, it does it with a slower pace compared to the first month (Fig. 23). This behaviour of the hydraulic head confirms what was already observed in the simulation of a single precipitation event, which

is that there is flow through the fault. Because of this, as the groundwater is flowing from the footwall to the hanging wall through the fault, the hydraulic head in each of the blocks has an opposite behaviour, decreasing in the footwall and increasing in the hanging wall. The last two months resemble the first two in terms of recharge rate, and therefore the response of the hydraulic head in each fault block is similar as those described before (Fig. 23). By the end of the simulation, the computed Δh in the footwall is 0.85 m, even though the highest computed Δh is 0.97 m by the end of the third month. In the hanging wall, by the end of the simulation, the computed Δh is 0.32 m, which also corresponds to the largest computed Δh throughout this simulation in this block of the fault. This indicates that even with relatively constant recharge rate, the hydraulic gradient variation across the fault is very dynamic.

Finally, a short span of time of 20 days was selected from the precipitation time series to simulate different precipitation events and assess the response of the model to them (Sc. H). As it can be observed in Figure 24, the hydraulic head in the footwall is very sensitive to the precipitation events, whereas the hydraulic head in the hanging wall does not show any direct response to them. As already observed in Sc. F, the response time to the moment of the recharge in this scenario is also fast for the footwall, and the hydraulic head peak occurs as well within less than 2 days. The increase of the hydraulic head in the footwall occurs mainly after large recharge rates (high precipitation events).

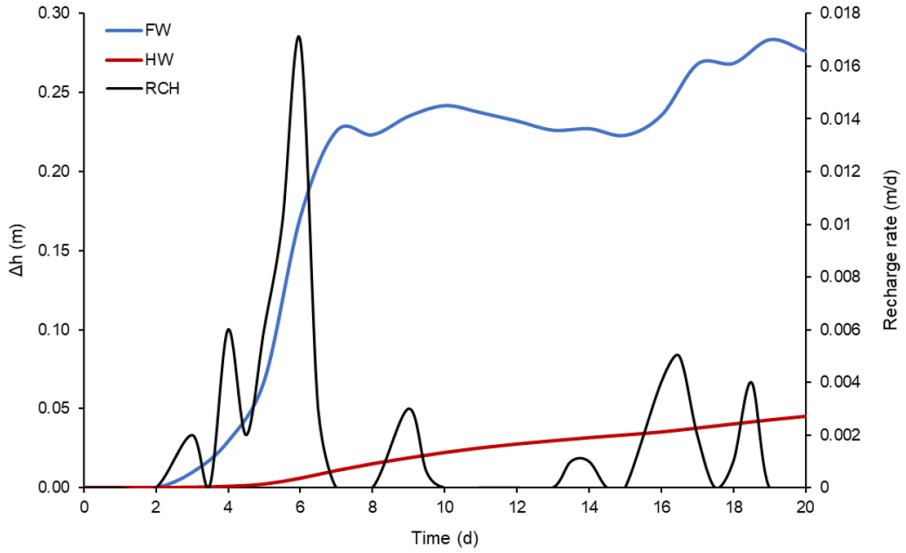

Figure 24. Computed hydraulic head difference (Δh) for a 20-day time series with realistic precipitation events (Sc. H). FW: footwall; HW: hanging wall; RCH: recharge rate.

4.1.4. Calibration of the 2D section against Maarlo data

The monitoring data of the piezometers installed on the Maarlo site was used from this point of the study on to perform a calibration, followed by a validation period. The calibration period was used to calibrate the hydraulic parameters of the formation and of the fault, as well as the recharge. The validation period was used to test if the calibrated parameters would allow to

reproduce a response similar to the observed data for another stress period (different precipitation pattern).

The calibration period consisted in 141 days (from 13th November 2015 to 31st March 2016), while the validation period consisted on 176 days (from April 1st to the 23rd of September of 2016), comprising thus the whole available data from the monitoring of the piezometers in Maarlo. The calibration was performed manually by means of the trial and error method trying to match both, the hydraulic head trend and the head difference between the two blocks of the fault, to the observed data. The parameters on which the calibration was performed were the fault's width and K_x, the different formation K_x and the recharge rate. The specific yield (S_y) and specific storage (S_s) terms from HCOV (Table 1) were fixed. The fault dip was set to be 90º as the ERT data shows a nearly vertical dipping fault (Deckers et al., 2018), and that the synthetic case study showed that 2 piezometers are not sufficient to resolve the dip (this will also be discussed later). The calibrated values are displayed in Table 7. As the hydraulic head could not be matched perfectly by calibrating these parameters, probably because of the fixed head boundary conditions used at both upstream and downstream limits that cannot accommodate variations of the hydraulic head, the focus was set on the head difference between the footwall and the hanging wall.

Table 7. Initial, calibrated and observed values of the different parameters.

Parameter		Initial value	Calibrated value	Observed value
Fault	Kx (m/d)	0.02	0.012	-
	width (m)	2.0	3.2	-
Meuse Gr. (HW)	Kx (m/d)	6.0	6.0	-
Mol Fm (HW)	Kx (m/d)	17.2	17.2	-
Mol Fm (FW)	Kx (m/d)	17.2	13.0	-
PB7	h_0 (m)	58.44	59.00	58.43
PB5	h_0 (m)	54.34	53.47	52.88

In order to calibrate the recharge rate, the footwall and the hanging wall were assigned different recharge patterns. In the footwall, at first, the recharge was simulated by a monthly average recharge. This approach did not match the observed fluctuations in the hydraulic head during the calibration period, but it showed the overall trend. In addition, as it has been showed before, once the recharge occurs, the response of the aquifer is fast and therefore, the observed data showed a delay compared with the computed one. This is because MODFLOW is not simulating the infiltration through the unsaturated zone. This problem was solved by imposing a delay of 10 days (estimated from the precipitation and hydraulic head time series of Maarlo) between the moment of the precipitation and the recharge. Moreover, to fit better the observed data and account for the dampening effect of the unsaturated zone, the recharge was averaged for periods of 48 h. In the hanging wall, however, the observed recharge patterns, which will be discussed further in this report, are different. Thus, the recharge rate was calibrated by delaying the moment of the recharge to ~80 days after the start of the simulation. This delay was also estimated from the time

series of hydraulic head and precipitation. Furthermore, the recharge rate was not simulated as in the footwall. Instead, a constant recharge rate was set to match the observed trend. The calibrated value of the recharge rate in the hanging wall is 0.0006 m/d. This approach is assumed valid as the thickness of the unsaturated zone is much larger in the hanging wall. As in Flanders much of the recharged occurs in the winter, the estimated amount of recharge from the precipitation (Fig. 25a) during the calibration period was set to be 65%, while in the validation period it was set to be 20%.

Although the computed hydraulic heads in the footwall and the hanging wall were higher than the observed ones, the initial head difference was properly matched, and its evolution throughout the simulation has a similar behaviour as in the observed data. The results of the calibration show that the computed hydraulic head follows the same general trend as the observed data, both in the footwall and the hanging wall, even though the smaller-scale fluctuations could not be simulated (Fig. 25b). The imposed delays helped matching the computed hydraulic head peaks with the data. The maximum increase of the hydraulic head in the footwall was 0.97 m, which makes the hydraulic head rise above the specified head in the boundary condition (59.90 m), creating a groundwater divide in the footwall, and thus, impacting flow behaviour. Therefore, the boundary conditions may have a significant impact on transient state simulations, and it will be discussed further in this report. During the validation period (day 141 to 317; Fig. 25b), the general trends computed are also matched with those observed. However, the hydraulic head increase is much smaller than the one observed. As the recharge was simulated as constant through time from day 80 and on, such a slight increase could be due to water flowing from the footwall to the hanging wall through the fault damage zone. Therefore, it would be impossible to simulate such a rise in the hydraulic head in the hanging wall without increasing the recharge rate at a given point in time during the validation period. This points out towards the need for an accurate characterization of the flow in the unsaturated zone to further improve the model. This will be discussed later.

Concerning the head difference between the two walls of the fault, the initial value (5.55 m) was matched accurately at 5.53 m. The computed trend during the calibration period is similar as the observed on the data from the monitoring (Fig. 25c). The maximum computed value for the head difference was 6.07 m, while in the observed data the maximum head difference between both walls is 6.56 m. However, the maximum computed and observed head differences do not occur at the same moment in time, showing a delay of 20 days between them (Fig. 25c). Most of the discrepancy can probably be explained by the approach used to simulate the recharge as the real data in the foot wall clearly show some fast reactions to some precipitation events. During the validation period, the computed and observed trends are similar. Nevertheless, the computed variation of the head difference shows a smoother increase and decrease compared with the monitoring data, even though it occurs in the same time interval (day 200 to 250).

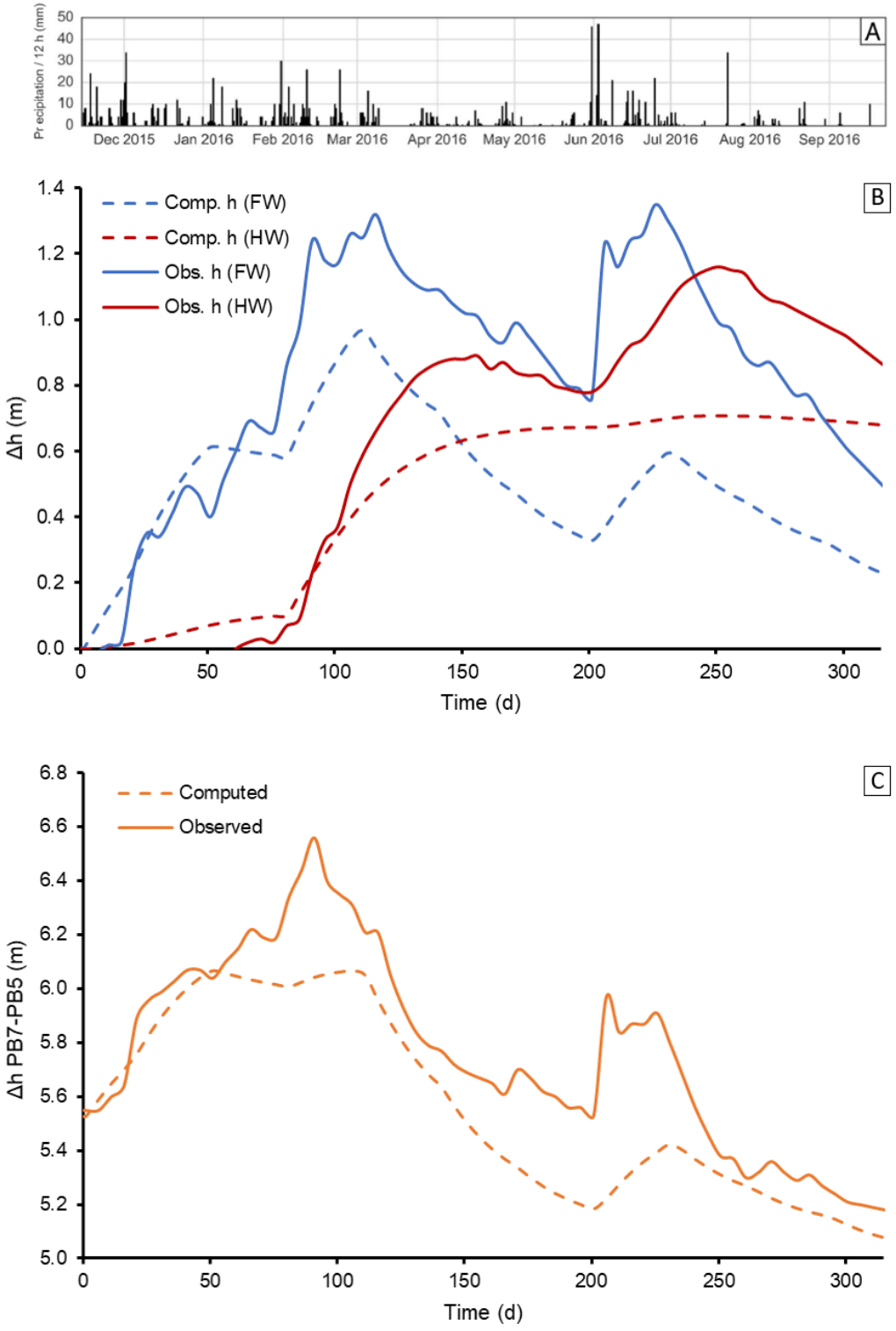

Figure 25. a) Precipitation data from the Kleine Brogel station averaged every 12h. b) Computed hydraulic head increase in the footwall and the hangingwall compared to the observed data. c) Computed and observed head difference between piezometers PB7 and PB5. The vertical scale has been exaggerated.

4.1.5. Discussion

Synthetic case

As observed in the results, the hydrogeological behaviour of a fault zone depends on various parameters which are correlated with each other. To begin with, the thickness and the bulk hydraulic conductivity of the fault zone define the specific resistance, directly dependent on the hydraulic conductivity and the width of the fault, (*c*; Eq. 1) to groundwater flowing orthogonally to the fault. This ratio is consistent with what has been observed in the output of the models. If either the thickness of the fault zone or the bulk hydraulic conductivity were decreased, the specific resistance decreased in accordance, implying a larger fluid mass flow through the fault zone, or for a fixed specific flux, a lower hydraulic gradient across the fault (Table 8). Therefore, smaller hydraulic head differences between the footwall and the hanging wall were observed. This can also be observed through Darcy's law (Eq. 2), where the width of the fault (equivalent to the length in Eq. 2) is inversely proportionally to the flux and directly proportional to the head difference (Δh) and thus, the hydraulic gradient across the fault zone. In addition, considering the fault zone as a heterogeneous whole, its equivalent (or bulk) hydraulic conductivity (K_{eq}; Eq. 8, defined for flow perpendicular to the fault) is also defined by the width of the damage zone:

$$K_{eq} = \frac{\sum_{i=1}^{n} dx_i}{\sum_{i=1}^{n} \frac{dx_i}{K_i}} \quad (8)$$

Where K_i is the hydraulic conductivity of zone i and dx_i the corresponding thickness. For these reasons, the thickness of the fault zone is considered as a crucial parameter in models with a continuum approach (Bense and Person, 2006; Bense et al., 2013). An influence of the ratio between the formation K_x and the fault K_x was also observed in the results. From this ratio it can be deduced that the bigger the difference between these parameters, the larger the hydraulic gradient is across the fault (Table 8). This relation may confirm that the absolute change is thus dependent on another parameter, probably the thickness of the fault zone as stated above. However, the general behaviour of groundwater will remain the same.

It has been observed in the results that the fault dip has a significant effect on the hydraulic gradient across the fault and the head difference between the footwall and hanging wall. Such an impact could be linked to the apparent horizontal width of the fault as the absolute thickness of the fault zone remained fixed for this test. It is interesting to note that a slight change in the horizontal width (e.g. Scenarios D1 and D4; Table 8) has a big impact on the gradient across the fault, which becomes smoother even though the specific resistance increases. As shown in Figure 21, the flow is mostly horizontal in the 2D model, so that the apparent width of the fault along the horizontal direction is increasing, when the fault is dipping more gently. This would mean that the simulated width of the fault zone in the model would increase as the inverse of the sine of the slope (Fig. 26; Eq. 9):

$$x = m \cdot \sin \alpha \quad (9)$$

Where *x* is the horizontal width, *m* the apparent horizontal width and *α* the dip angle of the fault. This approach provides a way to incorporate more easily dipping fault into regular grid, where steep dipping faults will be simulated with a smaller width than gentler dipping faults.

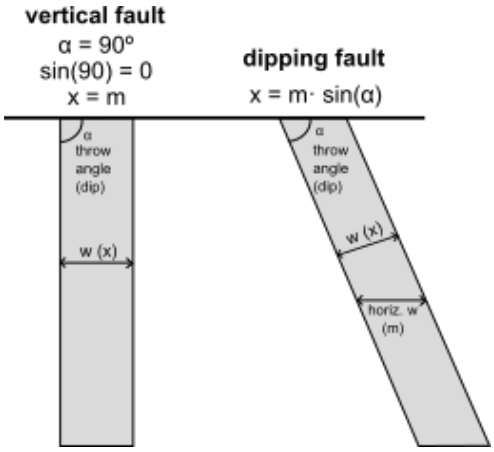

Figure 26. Schematic representation of the link between the horizontal width and the dip of the fault. The horizontal width varies as the sine of the throw angle.

Table 8. Calculation of the different ratios observed in the results. Δh/L represents the hydraulic gradient across the fault. c = specific resistance, K = hydraulic conductivity.

Scenario	Fault Kx (m/d)	Width (m)	Fm. Kx (m/d)	c (d)	Fm. K/ fault K	Δh/L
A1	0.005	4.0	0.6	800	120	-0.3966
A3	0.005	4.0	6.0	800	1200	-1.5341
A5	0.005	4.0	34.4	800	6880	-2.0546
B1	0.005	4.0	17.2	800	3440	-1.9178
B4	0.32	4.0	17.2	12.5	53.8	-0.2066
B7	20.48	4.0	17.2	0.2	0.8	-0.0035
C3	0.04	2.0	17.2	50	430	-1.2942
C6	0.04	0.2	17.2	5	430	-0.7776
D1	0.04	4.0	17.2	100	430	-0.8646
D4	0.04	4.6	17.2	115.5	430	-0.2902

The chosen boundary conditions, specially the specified-head (CHD) and the recharge rate (RCH), defined the general behaviour of the model and therefore, its effect will be discussed broadly. Although the limits of the model were pushed far enough of the zone of interest (around the fault) to limit the impact of the boundaries, its effects were still notable. First, setting a specified-head boundary at both ends of the model defined the regional gradient across the model. This option was initially chosen as it corresponds to the natural choice for the field application. With the implementation of the fault, the hydraulic gradient changes drastically throughout the cross-section. When conducting tests on the fault's K_x, the hydraulic head in the footwall raised above the value set as specified head for that boundary, as the fault was becoming a stronger flow barrier, preventing water recharging on the foot wall to easily flow to the hanging wall. Since the specified head boundary were chosen according to the corresponding field situation, this observation could be due to two reasons (or a combination of the two): (1) the upstream boundary condition is not realistic enough at such distance and should thus be increased, or (2) that the model cannot accommodate the input coming from the recharge for low

hydraulic conductivity value, and thus that the actual value is larger. A test with the specified-flow package as boundary condition in the footwall, was performed to investigate the response of this package and compare it to the response of the specified-head (Fig. 27). If the no-flow (specified flow = 0 m^3/d) boundary condition is used, the water table can rise with freedom in the footwall to accommodate the recharge and no maximum in the hydraulic head distribution is observed. This option might be more realistic, but then the distance of the boundary to the fault would play a role in the results as well. Although there is not a unique way to represent the boundaries of the model correctly, one should be aware of the role of the boundary conditions on the results of the sensitivity analysis. To limit its effect on the interpretation, in this study the focus is set on the behaviour close to the fault.

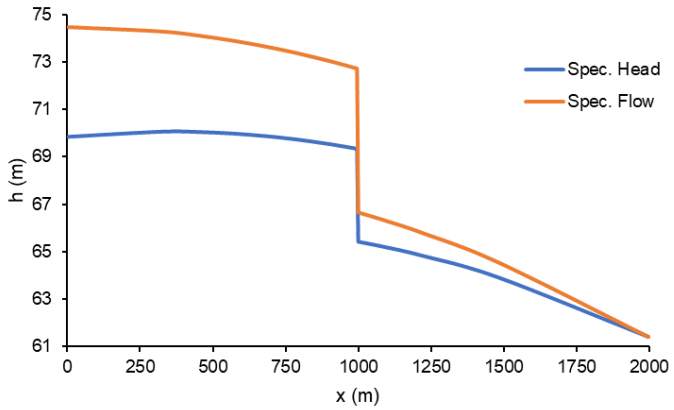

Figure 27. Results of the test with a no-flow and a specified head boundary condition. The boundary condition on the hangingwall remained as a specified head.

Field case

Lapperre et al. (2019) reviewed existing models in the RVG and showed that minor faults have values of the hydraulic resistance ranging from 5 to 500 days, while the major faults were fixed at 100,000 days. However, for a small-scale model like the proposed in this study (~2.5 km long), such a large resistance would be unrealistic as it would require a hundred-meter order of magnitude for the fault zone thickness if we assume a similar hydraulic conductivity. The achieved calibration value for the Maarlo case has a specific resistance of 266,7 days (w = 3.2 m and K_x = 0.012 m/d), which fits into the range for minor faults. The calibrated hydraulic conductivity falls as well in the ranges discussed by Lapperre et al. (2019) in their review (0,001 to 32 m/d). Moreover, the calibrated value matches the lowest values obtained from *in situ* measurements that have been performed in RVG faults: 0.012 m/d per 0.013 m/d respectively.

Problems related with the boundary conditions choice have arisen in transient state as well. The main problem was that the model was sensitive to the specified head in the hanging wall, which made the head difference between the two walls to small. Thus, by fixing the hanging wall value at the initial estimated level, the specified head in the foot wall could not rise enough to accommodate the observed increase of the hydraulic head after recharge event. The specified head in the hanging wall corresponds to the only location where water can flow out of the model

and is therefore important. By fixing it at a constant value in a transient simulation, one ignores that after precipitation events, the head at this boundary will probably rise as well. This surely influences the calibration process and induces some discrepancy. However, extending the model in that direction would require to push the boundary very far away from the fault, since there is no groundwater divide in the vicinity what would induce other problems (deviation from the 2D assumption). Possibly, a better calibration could be performed by adjusting the width and the hydraulic conductivity of the fault zone while maintaining the specific resistance fixed at 266,7 d.

Modelling the recharge rate in transient state for this specific case was also challenging. The response of the footwall and hanging wall to infiltration is very complex and thus, it could not be modelled with a single recharge pattern. Hill and Tiedeman (2007) discussed that recharge and the hydraulic conductivity are correlated and thus, calibrating both is almost impossible with only hydraulic head data. Therefore, it is important to provide a recharge rate as accurately as possible. Before taking this decision, a few tests were conducted to define the best way to model the recharge rate (Fig. 28) so that it reproduces the field observation. The results of these tests show that the best way of modelling the infiltration, in order to explain the observed behaviour on the field, was to only induce the recharge in the footwall. In that case, the level rises first in the footwall as a reaction to precipitation and then in the hanging wall through flow across the fault. Otherwise, if a similar recharge is imposed on both walls, the hydraulic head in the hanging wall rose to unrealistic high levels and therefore, such an approach was discarded as a modelling choice. However, in the field observations, the level in the hanging wall continues to rise to a level that cannot be explained by flow across the fault only. For long simulations, it is thus needed to consider a recharge rate on the hanging wall as well. The main difficulty probably comes from the different thickness of the unsaturated zone on both walls, as well as the presence of low hydraulic conductivity zones in the Meuse Group, delaying the recharge rate. This is the reason why different approaches were taken for the calibration. In order to simulate and calibrate the recharge patterns in a more accurate way, a better characterization of flow in the unsaturated zone would be required, which was not the goal of this study. Different modelling software such as HYDRUS 1D (Simunek et al., 2009) or the UZF package in MODFLOW (Niswonger et al., 2006) are available for simulating the unsaturated zone.

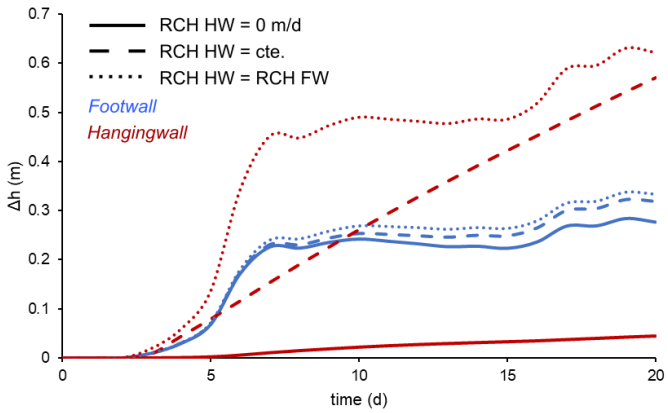

Figure 28. Results of the different approaches tested for modelling the recharge patterns observed in the field accurately.

Field data

The geophysical data acquired by Deckers et al. (2018) is very complete and allows a good representation of the geometry of the different hydrogeological domains and units. However, the groundwater data has been proved to be insufficient to determine the hydrogeological properties of the fault. To estimate the effect of the fault more accurately on the field, a distance of 114 m between the piezometers at each side of the fault segment has been proven to be too large. As it has been shown in the results of the synthetic case, for a vertical dipping fault, the steepest hydraulic gradient is restricted to the fault zone. If the fault is not vertical, the area where the head distribution is affected becomes larger into the hanging wall as the dip of the fault decreases, probably due to the horizontal width of the fault as discussed earlier. However, the maximum observed spread of the head distribution into the hanging wall was about 20 m for a dip of 60°, which is five times smaller than the distance between piezometers B1 and B2. With monitoring piezometers placed at such distances of each other in fault-controlled sites, it will be difficult to derive the fault zone K_x, its width and its dip if the gradient across the fault cannot be measured more accurately. Therefore, monitoring networks should be flexible to allow the installation of additional piezometers to further define the hydrogeological characteristics of the site (Singhal et al., 2009). This is the main reason why it was decided not to include the geometry of the fault in the calibration of the Maarlo site. The calibrated width of the fault can thus be regarded as an apparent horizontal width at the scale of the model.

For the Maarlo site specifically, as the fault does not present any structural complexity on the ERT data (Deckers et al., 2018), a large monitoring network would be unnecessary. However, as the fault is not believed to have a large damage zone, the target zone should be reduced to a decametric scale (tens of meters). As in the tests of the synthetic model approach a maximum spread of the gradient of 20 m was computed, this order of magnitude should be considered for the future installation of monitoring piezometers in this site or nearby. If the monitoring network in Maarlo was about to be expanded, the recommended target zone according to the results shown in this study should be around 15 to 30 m large. This target zone could also be valid for other sites along the GBF or any other fault if consistent field data is gathered.

4.2. Bree case

The knowledge obtained from the above-mentioned results was crucial in developing the 3D model for the Bree site. The latter was used to test four different fault-linking scenarios that could be possible for the GBF in this study area (see section 2.4). The four different scenarios consisted on a regional flow simulation (1; with no fault present) with a soft linked scenario (2), without any fault connection between the two GBF segments, a hard linked scenario (3) in which one of the segments is connected, and a hard link scenario in which both segments are connected on both sides (4).

4.2.1. Regional flow

For the first scenario, the groundwater flow regionally occurs towards the NE, as expected given the specified head at the boundaries (Fig. 29a). Using a fixed head boundary for the Bocholt fault is justified as the general regional gradient is towards the Meuse River, so that the flow component along the fault is negligible. This is also consistent with the conceptual model for the 2D case. The inclusion of the GBF into the model, however, alters this trend due to its behaviour as a flow barrier. The impact of such a flow barrier on groundwater flow generates a totally different response (Fig. 29b; Sc. 2-4). With the presence of the GBF, the groundwater flows mainly to the N, orthogonally to the fault. Through the fault, a large hydraulic gradient is generated, which results in a large head difference between the footwall and the hanging wall. Once the groundwater has reached the hanging wall, the flow changes from a mainly N direction to a NE direction. As the limit of the model was set to be the Bocholt fault, it is fair to assume that the flow direction in the hanging wall is orthogonal to the Bocholt fault. Furthermore, the Bocholt fault converges with the GBF a few hundred meters from the east margin of the model. This creates a steeper hydraulic gradient on the east margin compared to the west margin. These observations corroborate the observation that a larger fault step is observed in the eastern section of the GBF compared to its western section.

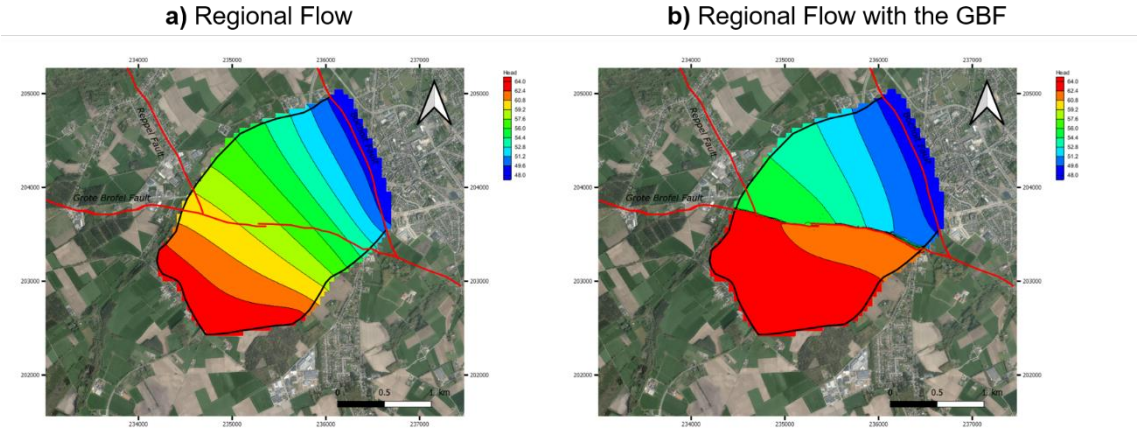

Figure 29. Piezometric maps defining the regional groundwater flow without the presence of the GBF (a) and with the presence of the GBF (b).

For each of the scenarios with the presence of the GBF (Sc. 2-4), the regional flow trends were perpendicular to both faults. First, to the GBF with a N direction in the footwall, and once groundwater has overcome the GBF and flows into the hanging wall, the flow becomes orthogonal to the Bocholt fault with a NE direction (Fig. 20b). Although the structural complexity created by the presence of the two GBF splays in the Bree site does not have any impact on such a large scale (~2.5 km), it has a significant impact on the groundwater flow behaviour at a local scale (~100 m). The result from the simulations of these different scenarios will be explained below.

4.2.2. Soft-linked fault scenario

In this scenario, the two segments of the GBF are not linked thus creating a ramp in the relay zone along which groundwater connection between the footwall and the hanging wall would still be possible, although quite narrow. The results from the simulation show that this connection between the two fault segments indeed induces a preferential flow path, allowing groundwater to flow from the footwall into the hanging wall with a parallel direction with respect to the fault splays (Fig. 30). In this simulation, F2 accommodates a rather small water table jump (~2 m) compared to F3 (~4.5 m; Fig. 31). This preferential flow path results in a smoother decrease of the water table in the hanging wall of F2.

The velocity vectors confirmed that the hanging wall of F2 acts as a preferential flow path. The computed velocities show that flow along the ramp in between F2 and F3 is faster than in the footwall and the hanging wall of the GBF (Fig. 30). The largest velocities in the hanging wall of F2 occur close to the fault splay F3. In addition, there is still flow occurring through both fault splays at a minor rate. In addition, the computed flow budget revealed that the flow transfer from the footwall to the hangingwall is markedly higher in the soft-link scenario than in the other scenarios: 361 m^3/d by ~91 m^3/d in both hard link set-ups. Thus, the rate of fluid mass flowing through the ramp in the hangingwall of F2 in a soft-linked scenario would be three times larger.

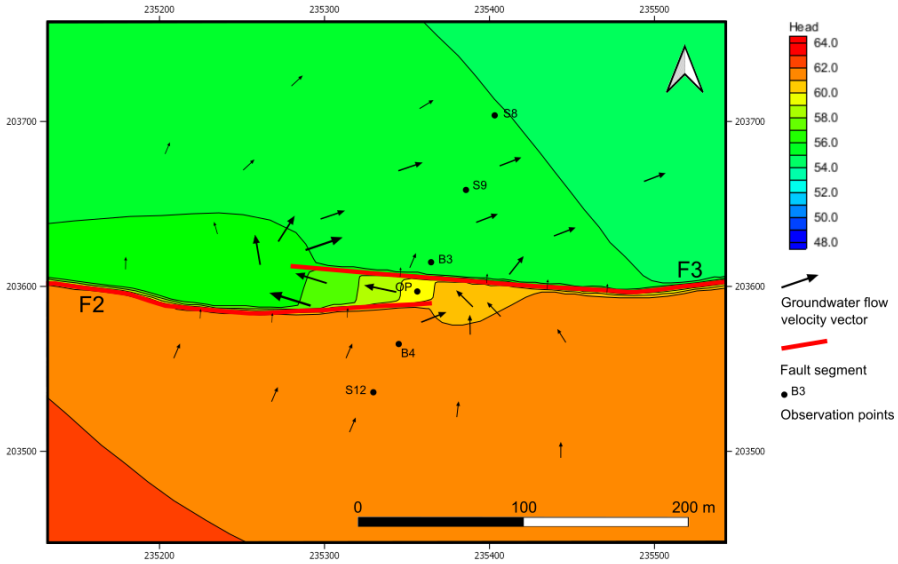

Figure 30. Hydraulic head map for a soft-linked fault scenario. The flow velocity vectors are displayed, and its length correspond to its magnitude.

4.2.3. Hard-linked fault scenarios

If the GBF segments were connected to each other, no preferential flow path would be expected in the area. As the link of the GBF segments in the Bree site is yet uncertain, two possibilities were considered as possible scenarios. In the first one, the fault would only be closed at one of the sides (Sc. 3), while in the second one, the fault would be closed at both sides (Sc. 4).

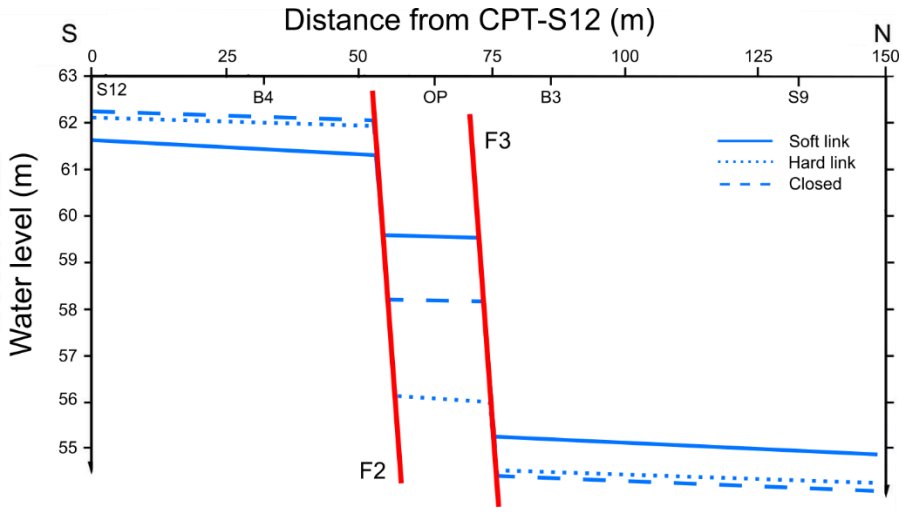

Figure 31. Cross section with the representation of the hydraulic heads computed in the observation points for each of the scenarios.

For scenario 3, the results show that there is not a preferential flow path if the segments are linked. In this case, the linked splay of the fault (F2) accommodates most of the hydraulic head difference between the footwall and the hanging wall (~6 m), while F3 only accommodates ~2 m (Fig. 31). However, in the side where the fault is not linked, the groundwater flows into the hanging wall with a smooth hydraulic gradient, accommodating this way the remaining head difference in this sector (Fig. 32). Velocity vectors show that most of the flow in this sector occurs through F2. Once groundwater has reached F2's hanging wall, the flow becomes parallel to the fault splays and its velocity increases as groundwater approaches the main hanging wall (Fig. 32).

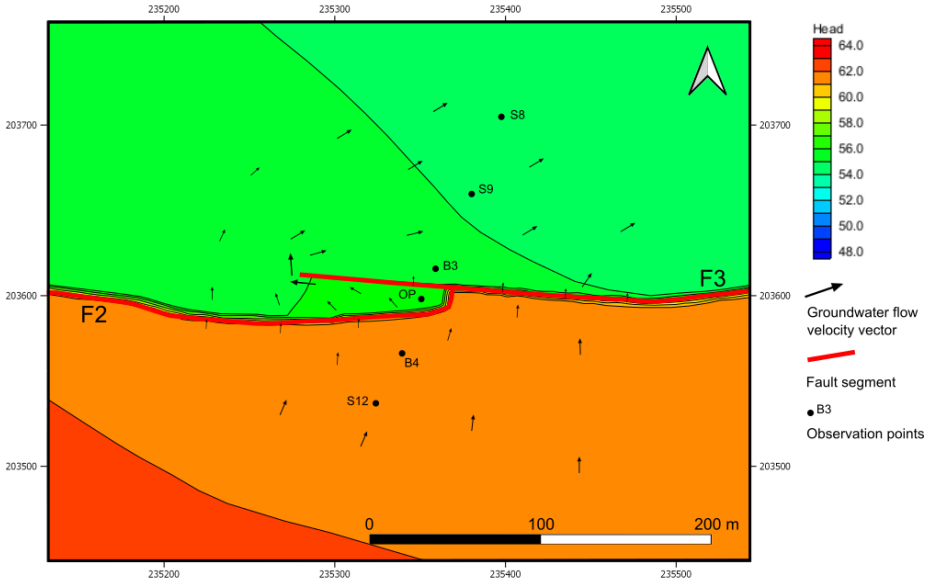

Figure 32. Hydraulic head map for a hard-linked fault scenario closed in the eastern side. The flow velocity vectors are displayed, and its length correspond to its magnitude.

If the GBF is linked at both sides (Sc. 4), the hydraulic head difference is accommodated by the two splays equally (~4 m each splay; Fig. 30). That is the main reason why the area closed by the fault shows an intermediate hydraulic head between the footwall and the hanging wall (Fig. 33). This area becomes thus, disconnected from the two walls of the fault as it is surrounded by flow-barriers. The velocity vectors show a homogeneous flow velocity throughout this area (Fig. 33). It is interesting to note that the geometry of the link not only influences the flow between the two splays but has also a slight influence on the regional hydraulic gradient.

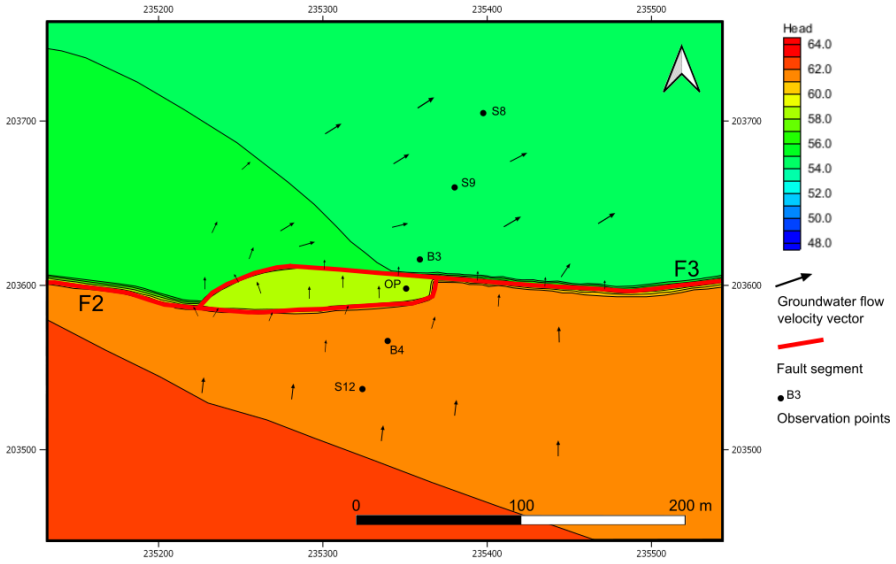

Figure 33. Hydraulic head map for a hard-linked fault scenario closed at both sides. The flow velocity vectors are displayed, and its length correspond to its magnitude.

4.2.4. Discussion

In contrast to the Maarlo site, the Bree site presents a complex geological structure with the presence of two different fault splays (F2 and F3). This structure controls the groundwater flow by creating a hydraulic head jump between the footwall and the hanging wall of at least 12 m (Deckers et al., 2018). As a calibration was not attempted for this case, the focus being on the effect of the link between splays, a jump of 12 m between both walls was not achieved by the simulation. Nevertheless, following the recommendations of the synthetic case, calibration should be achievable in a limited time frame. However, the groundwater flow behaviour could be observed through the different proposed scenarios considering the three-dimensionality of the fault structure. Micarelli et al. (2006) already used groundwater modelling tools with a continuum approach for the fault zones to determine their three-dimensional structure.

It has been observed in the results that in the hangingwall of F2, flow can occur parallel to both fault splays (Sc. 2 and 3). This behaviour was also observed by Micarelli et al. (2006), who found out in their study that water tends to flow preferentially parallel to bedding. However, when water encounters a transversally impermeable fault, it flows parallel to the main faults up to the next relay, crossing the fault zone in these relays between two fault segments (Micarelli et al., 2006). The results of this study show as well that the groundwater behaviour depends on how the fault

segments are linked, as different responses were computed depending on the type of link. It is fair to assume then, that groundwater field observations and modelling can be a helpful tool to determine the geological structure of the fault as previously demonstrated by Micarelli et al. (2006). Nevertheless, an extensive monitoring network would be necessary to characterize the groundwater behaviour accurately.

Deckers et al. (2018) monitoring network consisted only of two piezometers and groundwater level determination in the CPTs and HA borings, all of them along a cross section perpendicular to the fault. Observing the three-dimensional groundwater flow behaviour on a cross section is not possible and thus, it is not enough to precisely characterize the Bree site hydrogeologically. By such a disposition, the flow parallel to the fault in the relay cannot be recorded. Nevertheless, the additional observation point located at the hanging wall of F2 showed that the head jump is different for each of the scenarios (Fig. 30). This observation point corresponds broadly to the HA borings HA4 and HA5, in which Deckers et al. (2018) observed a small groundwater step (~1 m) compared to the one caused by fault splay F3 between HA5 and HA6. The simulated response of the soft-link scenario was quite similar, with a smaller step of the groundwater table in F2 compared to F3. This suggests that the type of link between both fault splays may be a soft link with an associated ramp that would act as a preferential flow path. However, with a single additional piezometer or the HA borings it is still difficult to determine completely the structure of the fault and the groundwater flow behaviour. Thus, installing piezometers parallel to the fault segment and perpendicular to the already existing cross section would point out how this parallel flow occurs, delineating the three-dimensional structure of the fault. Furthermore, the regional flow is slightly affected by the presence of these local complexities and it could be monitored by creating a network with the installation of several piezometers spread through the footwalls and hangingwalls of the major faults.

The velocity vectors computed in the different scenarios show that not only the hydraulic head is changing, but also the velocity of the flow changes in each scenario. Therefore, flux measurements or tracing experiments could also be useful to elucidate the problem. In terms of application, the type of link could have implications for pumping activities and contaminant transport (Bense et al., 2013) as the amount of water flowing from the footwall to the hangingwall is larger with a soft-linked fault than with a hard-linked fault.

5. Conclusions

Various numerical model exercises have been conducted in this study to comprehend better the effect of fault zones in shallow groundwater systems and apply it to a field investigation of the GBF. A preliminary sensitivity analysis on the parameters controlling the fault's hydrogeological behaviour was performed in a synthetic case (based on the Maarlo Site) to allow the identification of those parameters which exert a larger control on the groundwater flow. The results of the sensitivity analysis confirm that the thickness of the fault zone is the most crucial parameter as already stated by Bense and Person (2006) and Bense et al. (2013). In addition, the bulk hydraulic

conductivity of the fault zone was also found to be a determining parameter as together with the width of the fault zone, they define the resistance to groundwater flow. It was also found out that the contrast between the hydraulic conductivities of the geological formations and the fault zone has an impact on the steepness of the hydraulic gradient across the fault.

The synthetic case and the knowledge gained through the different simulations, were transposed to a real cross-section model to perform a calibration with the monitoring data from Maarlo. The response of the aquifer to infiltration could be accurately modelled. However, various modelling choices regarding the boundary conditions had to be made. The specified-head boundary at the edges of the model was proven to be the best option. Nevertheless, its fixed value prevented the water table to rise as much as the response observed in Maarlo. The recharge rate was calibrated manually by setting a delay of 10 days in the footwall and 80 days in the hangingwall. Furthermore, the recharge rate for both walls was different as in the hangingwall a constant recharge rate was set to model its response. For these reasons, the unsaturated zone flow should be better characterized to model the difference in the responses of the footwall and the hangingwall.

The Bree case proved that the geological structure of faults could be determined by groundwater level observation, as Micarelli et al. (2006) already showed in their study. The groundwater flow response on each of the scenarios was different and it could be recorded in the field by a monitoring network with several piezometers. As for the different scenarios, a soft link between the fault splays generates a preferential flow path from the footwall to the hangingwall, where the velocity of the groundwater flow is larger than across the fault. Whereas in both hard link scenarios, the main segment of the fault generated a large gradient across the fault zone and no preferential flow path could be observed. The results from the scenarios together with the observations of Deckers et al. (2018) on HA borings, suggest that the most probable structure is a soft-linked fault.

Although the hydraulic data of the zone was insufficient, numerical models that represented the conditions of both sites could be built to analyse the hypothetical flow responses. With regards to these generated responses in the model, guidelines for field data acquisition can be derived from them. For simple structural settings, the distance between piezometers in each of the walls is very important to derive the geometry and properties of the fault. For restricted fault damage zones, the piezometers should not be placed at distances greater than ~30 m. Otherwise, it would be impossible or, at least, very difficult to derive the properties of the fault. For geologically complex structural sites however, the distance between boreholes is not a crucial factor but an extensive monitoring network specifically designed for the site. The results of the different scenarios covered for the Bree site, show specifically for this site that additional piezometers should be placed parallel to the fault splays (F2 and F3). In addition, piezometers spread through the footwall and hangingwall of the GBF could also add valuable information into understanding the groundwater flow behaviour.

6. References

Aquaveo (2018). Aquaveo, L.L.C., 2007. Groundwater Modeling System Version 10.4, UT, USA.

Bear, J., & Cheng, A. H.-D. (2010). Modeling Groundwater Flow and Contaminant Transport. In *Modeling Groundwater Flow and Contaminant Transport*. Springer Netherlands. 813p. https://doi.org/10.1007/978-1-4020-6682-5

Beerten, K., Vandenberghe, N., Gullentops, F., & Paulissen, E. (2005). *Quartairgeologische kartering - Maaseik 10-18*. Vlaamse overheid Dienst Natuurlijke Rijkdommen.

Bense, V. F., Gleeson, T., Loveless, S. E., Bour, O., & Scibek, J. (2013). Fault zone hydrogeology. *Earth-Science Reviews*, *127*, 171–192. https://doi.org/10.1016/j.earscirev.2013.09.008

Bense, V. F., & Person, M. A. (2006). Faults as conduit-barrier systems to fluid flow in siliciclastic sedimentary aquifers. *Water Resources Research*, *42* (5), 1–18. https://doi.org/10.1029/2005WR004480

Bense, V. F., Van Balen, R. T., & De Vries, J. J. (2003). The impact of faults on the hydrogeological conditions in the Roer Valley Rift System: An overview. *Geologie En Mijnbouw / Netherlands Journal of Geosciences*, *82* (1), 41–54. https://doi.org/10.1017/S0016774600022782

Bense, V. F., Van den Berg, E. H., & Van Balen, R. T. (2003). Deformation mechanisms and hydraulic properties of fault zones in unconsolidated sediments; the Roer Valley Rift System, The Netherlands. *Hydrogeology Journal*, *11* (3), 319–332. https://doi.org/10.1007/s10040-003-0262-8

Bense, V., & Van Balen, R. (2003). Hydrogeological aspects of fault zones on various scales in the Roer Valley Rift System. *Journal of Geochemical Exploration*, *78–79*(APRIL), 317–320. https://doi.org/10.1016/S0375-6742(03)00031-1

Caine, J. S., Evans, J. P., & Forster, C. B. (1996). Fault zone architecture and permeability structure. *Geology*, *24* (11), 1025–1028. https://doi.org/10.1130/0091-7613(1996)024<1025:FZAAPS>2.3.CO;2

Camelbeeck, T., & Meghraoui, M. (1998). Geological and geophysical evidence for large palaeo-earthquakes with surface faulting in the Roer Graben (northwest Europe). *Geophysical Journal International*. https://doi.org/10.1046/j.1365-246x.1998.00428.x

Deckers, J. (2016). The Late Oligocene to Early Miocene early evolution of rifting in the southwestern part of the Roer Valley Graben. *International Journal of Earth Sciences*, *105* (4), 1233–1243. https://doi.org/10.1007/s00531-015-1236-5

Deckers, J., Van Noten, K., Schiltz, M., Lecocq, T., & Vanneste, K. (2018). Integrated study on the topographic and shallow subsurface expression of the Grote Brogel Fault at the boundary of the Roer Valley Graben, Belgium. *Tectonophysics*, *722*, 486–506. https://doi.org/10.1016/j.tecto.2017.11.019

DOV (2003a). *Put 931/23/7 (meetnetput)*. https://www.dov.vlaanderen.be/data/put/2017-002239#3

DOV (2003b). *Put 935/23/16a (meetnetput)*. https://www.dov.vlaanderen.be/data/put/2017-002265#3

Dusar, M., Rijpens, J., Sintubin, M., & Wouters, L. (2001). Plio-Pleistocene fault pattern of the Feldbiss fault system (Southern border of the Roer Valley Graben, Belgium) based on high resolution reflection seismic data. *Geologie En Mijnbouw/Netherlands Journal of Geosciences*, *80* (3–4), 79–93. https://doi.org/10.1017/s0016774600023751

Fulljames, J. R., Zijerveld, L. J. J., & Franssen, R. C. M. W. (1997). Fault seal processes: systematic analysis of fault seals over geological and production time scales. *Norwegian Petroleum Society Special Publications*, *7* (C), 51–59. https://doi.org/10.1016/S0928-8937(97)80006-9

Geluk, M. C., Duin, E. J. T., Dusar, M., Rijkers, R. H. B., Van Den Berg, M. W., & Van Rooijen, P. (1994). Stratigraphy and tectonics of the Roer Valley Graben. *Geologie En Mijnbouw*, *73* (2–4), 129–141.

Gorelick, S. M. (1983). A review of distributed parameter groundwater management modeling methods. *Water Resources Research*, *19* (2), 305–319. https://doi.org/10.1029/WR019i002p00305

Harbaugh, Arlen, W. (2005). MODFLOW-2005 , The U . S . Geological Survey Modular Ground-Water Model — the Ground-Water Flow Process. *U.S. Geological Survey Techniques and Methods*, 253.

Harte, P. T., Konikow, L. F., & Hornberger, G. Z. (2006). Simulation of solute transport across low-permeability barrier walls. *Journal of Contaminant Hydrology*, *85* (3–4), 247–270. https://doi.org/10.1016/j.jconhyd.2006.02.012

Heynekamp, M. R., Goodwin, L. B., Mozley, P. S., & Haneberg, W. C. (1999). *Controls on fault-zone architecture in poorly lithified sediments, Rio Grande Rift, New Mexico: Implications for fault-zone permeability and fluid flow* (pp. 27–49). https://doi.org/10.1029/gm113p0027

Hill, M. C., & Tiedeman, C. R. (2007). Effective Groundwater Model Calibration. In *Effective Groundwater Model Calibration*. John Wiley & Sons, Inc. https://doi.org/10.1002/0470041080

Hornerberg, P.A.; Konikow, L.F., Harte, P. T. (2002). Simulating Solute Transport Across Horizontal-Flow Barriers Using the MODFLOW Ground-Water Transport Process. *U.S. Geological Survey Open-File Report 02-52, 18p.*

Hsieh, P.A.; Freckleton, J. R. (1993). Documentation of a Computer Program To Simulate Horizontal-Flow Barriers Using Ground-Water Flow Model. *U.S. Geological Survey Open-File Report 92-477*, 32 p.

Knipe, R. J. (1993). The influence of fault zone processes and diagenesis on fluid flow. *Diagenesis and Basin Development*, 135–151.

Konikow, L. F., & Bredehoeft, J. D. (1992). Ground-water models cannot be validated. *Advances in Water Resources*, *15*(1), 75–83. https://doi.org/10.1016/0309-1708(92)90033-X

Lapperre, R. E., Kasse, C., Bense, V. F., Woolderink, H. A. G., & Van Balen, R. T. (2019). An overview of fault zone permeabilities and groundwater level steps in the Roer Valley Rift System. *Netherlands Journal of Geosciences*, *98*. https://doi.org/10.1017/njg.2019.4

Lebbe, L. & A. Vandenbohede, 2004. Ontwikkeling van een lokaal axi-symmetrisch model op

basis van de HCOV-kartering ter ondersteuning van de adviesverlening voor grondwaterwinningen. Studie in opdracht van AMINAL, afdeling Water, 23 pag. + bijlagen.

Loudyi, D. (2005). 2D finite volume model for groundwater flow simulations : integrating non-orthogonal grid capability into modflow. *Ph.D Thesis, Cardiff University, 241p.*

Meyus, Y., Batelaan, O., & De Smedt, F. (2000). Hydrogeologische Codering van de Ondergrond van Vlaanderen (HCOV). *Onderzoeksopdracht voor het Ministerie van de Vlaamse Gemeenschap Departement Leefmilieu en Infrastructuur Administratie Milieu-, Natuur-, Land- en Waterbeheer afdeling Water AMINAL, Brussel*, 58p.

Micarelli, L., Moretti, I., Jaubert, M., & Moulouel, H. (2006). Fracture analysis in the south-western Corinth rift (Greece) and implications on fault hydraulic behavior. *Techtonophysiscs*, *426*, 31–59. https://doi.org/10.1016/j.tecto.2006.02.022

Michon, L., & Van Balen, R. T. (2005). Characterization and quantification of active faulting in the Roer valley rift system based on high precision digital elevation models. *Quaternary Science Reviews*, *24* (3-4 SPEC. ISS.), 455–472. https://doi.org/10.1016/j.quascirev.2003.11.009

Niswonger, R. G., Prudic, D. E., & Regan, S. R. (2006). Documentation of the Unsaturated-Zone Flow (UZF1) Package for Modeling Unsaturated Flow Between the Land Surface and the Water Table with MODFLOW-2005. *U.S. Geological Survey Techniques and Methods 6-A19, 62 p.*

Paulissen, E. (1997). Quaternary morphotectonics in the Belgian part of the Roer Graben. In *Aardkundige Mededelingen* (Vol. 8, pp. 131–134).

Rawling, G. C., Goodwin, L. B., & Wilson, J. L. (2001). Internal architecture, permeability structure, and hydrologic significance of contrasting fault-zone types. *Geology*, *29* (1), 43–46. https://doi.org/10.1130/0091-7613(2001)029<0043:IAPSAH>2.0.CO;2

Schokker, J., & Koster, E. A. (2004). Sedimentology and facies distribution of Pleistocene cold-climate aeolian and fluvial deposits in the Roer Valley Graben (southeastern Netherlands). *Permafrost and Periglacial Processes*, *15* (1), 1–20. https://doi.org/10.1002/ppp.477

Scholz, C. H. (2002). The Mechanics of Earthquakes and Faulting. In *The Mechanics of Earthquakes and Faulting*. Cambridge University Press. https://doi.org/10.1017/cbo9780511818516

Simunek, J., Huang, K., Sejna, M. y van Genuchten, M. T. (2009). The HYDRUS-1D software package for simulating the one-dimensional movement of water, heat and multiple solutes in variable-saturated media. Dep. Environ. Sci., Univ. of California Riverside, Riverside, CA. 332p.

Singhal, B. B. S., & Gupta, R. P. (2010). Applied hydrogeology of fractured rocks: Second edition. In *Applied Hydrogeology of Fractured Rocks: Second Edition*. Springer Netherlands. 408p. https://doi.org/10.1007/978-90-481-8799-7

Singhal, N., Samaranayake, R., Gunasekera, H. D., & Islam, J. (2009). Groundwater Monitoring. In *ENVIRONMENTAL MONITORING: Vol. II* (p. 25).

Turnadge, C., Mallants, D., Peeters, L., & Land, C. (2018). *Overview of aquitard and geological fault simulation approaches in regional scale assessments of coal seam gas extraction*

impacts. Commonwealth Scientific and Industrial Research Organisation (CSIRO), Canberra.

Vandenberghe, N., Burleigh Harris, W., Wampler, J. M., Houthuys, R., Louwye, S., Adriaens, R., Vos, K., Lanckacker, T., Matthijs, J., Deckers, J., Verhaegen, J., Laga, P., Westerhoff, W., & Munsterman, D. (2014). The implications of K-Ar glauconite dating of the diest formation on the paleogeography of the upper miocene in Belgium. *Geologica Belgica*, *17* (2), 161–174.

Vandenbohede, A., & Lebbe, L. (2006). Occurrence of salt water above fresh water in dynamic equilibrium in a coastal groundwater flow system near De Panne, Belgium. *Hydrogeology Journal*, *14* (4), 462–472. https://doi.org/10.1007/s10040-005-0446-5

Vanneste, K., Camelbeeck, T., & Verbeeck, K. (2013). Model of composite seismic sources for the Lower Rhine Graben, northwest Europe. *Bulletin of the Seismological Society of America*, *103* (2 A), 984–1007. https://doi.org/10.1785/0120120037

Vanneste, K., Verbeeck, K., Camelbeeck, T., Paulissen, E., Meghraoui, M., Renardy, F., Jongmans, D., & Frechen, M. (2001). Surface-rupturing history of the Bree fault scarp, Roer valley graben: Evidence for six events since the late Pleistocene. *Journal of Seismology*. https://doi.org/10.1023/A:1011419408419

VMM (2004). *DHM-Vlaanderen, raster, 5 m | Geopunt Vlaanderen*. http://www.geopunt.be/catalogus/

VMM (2008). Grondwater in Vlaanderen: het Maassysteem. Vlaamse Milieumaatschappij. Aalst. 95 p.